5-2018

Harmonic Detection and Selectively Focusing Electromagnetic Waves onto Nonlinear Targets using Time-Reversal

Joseph Michael Faia

Harmonic Detection and Selectively Focusing Electromagnetic Waves onto Nonlinear Targets using Time-Reversal

A Thesis

Submitted to the Faculty

of

Rose-Hulman Institute of Technology

By

Joseph Michael Faia

In Partial Fulfillment of the Requirements for the Degree of Master

of

Science in Electrical Engineering

May 2018

ROSE-HULMAN INSTITUTE OF TECHNOLOGY

Final Examination Report

Joseph Faia — Name

Electrical Engineering — Graduate Major

Thesis Title **Harmonic Detection and Selectively Focusing EM Waves onto Nonlinear Targets Using Time-Reversal**

DATE OF EXAM: April 19, 2018

EXAMINATION COMMITTEE:

	Thesis Advisory Committee	Department
Thesis Advisor:	Edward Wheeler	ECE
	Yong Jin Kim	ECE
	Scott Kirkpatrick	PHOE
	Sun Hong	

PASSED X **FAILED** ____

ABSTRACT

Faia, Joseph Michael

M.S.E.E.

Rose-Hulman Institute of Technology

May 2018

Harmonic Detection and Selectively Focusing Electromagnetic Waves onto Nonlinear Targets using Time-Reversal

Thesis Advisor: Dr. Edward Wheeler

Ultra-wide band radar is a growing interest for the enhanced capability of ranging, imaging, and multipath propagation. An ultra-wide band pulse imposed on a system provides a near impulse like response and is, therefore, more descriptive than a conventional monotonic pulse. Combining pulse inversion with ultra-wide band DORT (a French acronym for the decomposition of the time reversal operator) is a technique which could be used to for greater visibility of nonlinear targets via harmonic detection in the presence of larger linear scatterers. Energy can be selectively focused onto nonlinear scatterers in complex, inhomogeneous environments. This thesis[1], will expand upon previous work, and demonstrate nonlinear detection and selective focusing with pulse inversion combined with DORT.

[1] This thesis builds on conference paper published and presented at URSI GASS 2017 in Montreal, Canada and forms the basis for a journal paper to be submitted this Spring.

DEDICATION

This thesis is dedicated to my parents Dan and Dawn Faia for their unwavering love and support.

Thank you for providing the opportunity and encouragement to pursue my education in Electrical Engineering

ACKNOWLEDGEMENTS

This thesis would not have been possible without the guidance and expertise brought by Dr. Sun Hong. I would like to thank him for introducing me to this project and working with me. I would also like to thank Dr. Ed Wheeler for his support of the work in this thesis. I would like to thank Yuije “Tao” He and Matthew Howlett who were huge contributors in the setup of the experiment and development of the experimental procedure. Finally, I owe a lot to the ECE Department technicians Jack Shrader, Garry Meyers, and Mark Crosby for their time and efforts in ensuring that we had everything we needed for this investigation.

TABLE OF CONTENTS

TABLE OF FIGURES

LIST OF ABBREVIATIONS

TR	Time-reversal
TRM	Time-reversal mirror
NL	Nonlinear
PI	Pulse inversion
DORT	French acronym for decomposition of the time-reversal operator
EM	Electromagnetic
EVD	Eigenvalue decomposition
SVD	Singular value decomposition
TRO	Time-reversal operator
MDS	Minimum discernable signal
DNR	Dynamic range
UWB	Ultra-wide band
VNA	Vector network analyzer
CST MWS	Computer Simulation Technology – Microwave Studio®
RF	Radio frequency

LIST OF SYMBOLS

English symbols

$\underline{\boldsymbol{E}}$	Electric field vector in the electromagnetic wave equation
$\boldsymbol{M}$	Multi-static data matrix
$\boldsymbol{H}$	Transfer matrix
f	Frequency (in Hertz)
t	Time (in seconds)
m	Meters
l	Path length
d	Array spacing

Greek Symbols

λ	Wavelength
ω	Frequency (in radians per second)
ε	Permittivity of the medium
μ	Permeability of the medium
φ	Angle of target off of the normal vector of the array

GLOSSARY

Harmonics	Spectral copies of frequency response, occurs at integer multiples of the fundamental frequency
Time-reversal	The response of the data y(t) has a time-reversal response of y(-t)
Multi-static	The dataset which consists of a matrix containing all possible mono-static and bi-static combinations
Mono-static	The dataset in which the transmit and receive antenna are the same
Bi-static	The dataset in which the transmit and receive antenna are different
Greens function	Describes the impulse response of a system in both space and time
Eigenvalues	Scalar values that are characteristic to a set of differential equations
Eigenvectors	A vector that when operated on by a given operator gives a scalar multiple of itself

1. INTRODUCTION

Developing the means to more efficiently and effectively detect and locate targets of interest using electromagnetic waves has important applications ranging from wireless power transfer to cancer detection to threat identification, all of which become significantly more difficult in an inhomogeneous environment. In the work reported here, techniques originally developed for use in acoustics are adapted to detect targets acting as non-linear scatterers of electromagnetic waves.

In the early 1990's, Mathias Fink from the University of Paris developed a technique using time-reversal (TR) which allows a broadband signal from an acoustic point source to be detected by an array of sensors, for this received signal to then be modified via TR to create a signal to be fed back as the excitation to the acoustic array which results in a signal which focuses at the location of the original point source, thereby allowing the acoustic array to act as a time-reversal mirror (TRM) [1].

The next stage of refinement was realized when the array was allowed to act as original excitation with the scattered signal from a target serving the role of point source. This was a crucial step in that it allowed Fink's PhD student Claire Prada to use the array as excitation to multiple targets which then act as multiple scatterers. Together Prada and Fink developed a powerful technique allowing for selective focusing on multiple targets, a technique known as decomposition of the time-reversal operator (known as DORT after the French acronym) [2]. Since all this work ultimately rests on the fact that acoustic waves are governed by the wave equation, these techniques originally developed for acoustics can also be used in investigations involving electromagnetic (EM) waves [3].

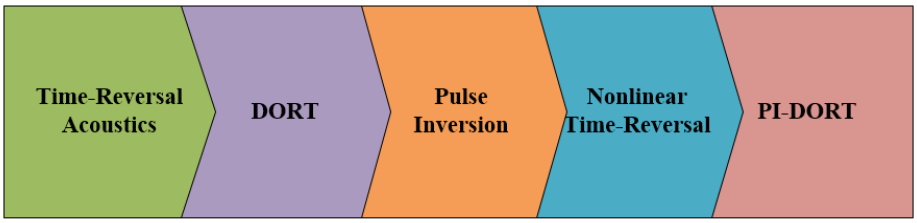

Figure 1.1: Timeline for the Development of PI-DORT

In this report, DORT is used in the identification of targets which scatter EM waves, specifically on targets having non-linear (NL) characteristics such as diodes and transistors which scatter waves with harmonics of the excitation frequencies. The main obstacle in attempting to detect such NL targets in a complex environment of linear clutter (e.g., furniture, trees, and buildings) is that the NL signals, particularly the harmonic responses, are often orders of magnitude smaller than the waves scattered from linear targets. It is shown that summing the responses from two broadband time-domain pulses, with one an inverted version of the other, results in the odd-order harmonics, including the fundamental, to be largely removed while at the same time enhancing the even-order harmonics. The aim of this work is to show that using DORT together with pulse inversion (PI) allows relatively small nonlinear targets to be distinguished in a complex environment, even one involving much larger linear targets [4].

The work presented in this thesis combines the use of ultra-wide band DORT and PI to detect and selectively focus on NL targets in complex propagation environments. The simulation and experimental results presented in this thesis provide substantial validation of PI DORT theory with potential applications in defense, medicine, security, wireless power transfer and communications.

2. BACKGROUND

Using conventional radar techniques it can be difficult to detect and focus energy onto a target in an inhomogeneous (complex) environment. It would be an important step if this difficulty could be overcome since, in many real-world applications, the medium will be complex – which indoors could include the clutter of electronics, household goods and office furniture and outdoor would include a range of buildings, vehicles, plants, and animals. In this section, the analytical foundations will be developed to support the models, simulations, and measurements developed within the work of this thesis.

Time-Reversal Invariance of the Lossless Wave Equation

The propagation of a plane wave is governed by the lossless wave equation (2.1). The lossless wave equation is invariant under time-reversal because the time derivative is second order. In order for the time-reversal technique to be possible, it must hold true that if $E(\underline{\boldsymbol{r}}, t)$ is a solution to the wave equation then $E(\underline{\boldsymbol{r}}, -t)$ must also be a solution. To show that this is true we start with the general lossless, source-free wave equation

$$\nabla^2 \underline{\boldsymbol{E}} - \mu\varepsilon \frac{\partial^2 \underline{\boldsymbol{E}}}{\partial t^2} = 0 \tag{2.1}$$

Since the wave equation contains only a second derivative as an operator on time, the solution to the wave equation must have symmetry in time.

Time-reversal invariance of the lossless wave equation implies reciprocity thereby allowing a received wave to be backtracked through the inhomogeneous medium so that that the original signal may be reconstructed at the original source location. The invariance of the wave equation under has been exploited in acoustics and, more recently, in electromagnetics.

Generated Harmonics of Nonlinear Systems

Nonlinear distortion refers to the relationship between the input and output signals of a nonlinear system and presents in two different forms, asymmetrical and symmetrical. The terms come from types of distortion resulting from sinusoidal excitation, where symmetric NL distortion results in symmetric distortion for the positive and negative portions of the sinusoid and asymmetric NL distortion resulting in asymmetric distortion. Asymmetrical distortion is often found in semiconductor devices such as diodes and transistors, the building blocks of electronics. The asymmetry refers to the distortion across the center axis of the signal as shown in Figure 2.1. Excitation of asymmetrical distortion nonlinear targets exhibit harmonics in their scattered responses for asymmetrical distortion there are even and odd order harmonics present.

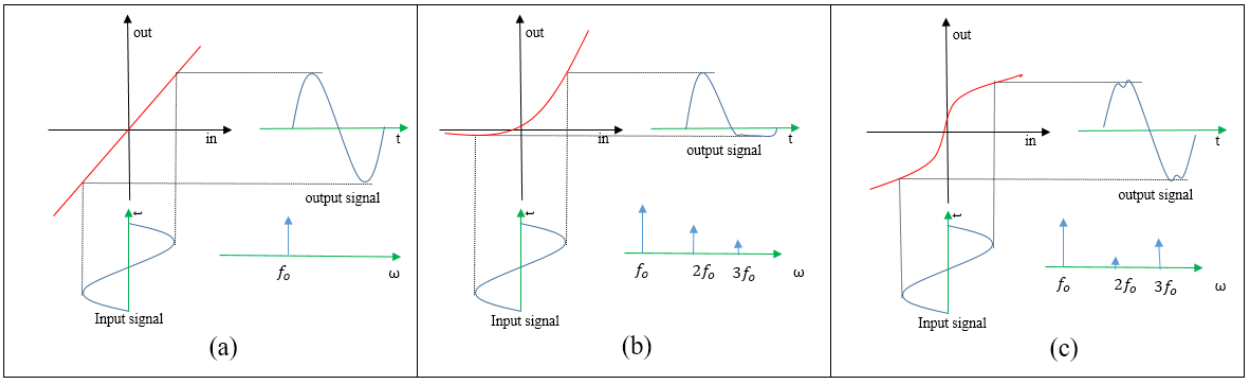

Figure 2.1: Illustration of the response of a (a) linear system, (b) asymmetric distortion nonlinear system and (c) symmetric distortion nonlinear system

NL targets with symmetrical distortion present stronger odd order harmonics when excited. This means the band of a finite bandwidth pulse will repeat itself on odd integer multiples (3ω, 5ω, etc.) of the center frequency, shown in Figure 2.1. The nonlinear targets identify themselves on this principle. The detection of harmonics is often made difficult since their magnitude is typically significantly smaller than the fundamental peaks given by linear scatterers (by an order of magnitude or more). This becomes a significant problem in the context of dynamic range.

Schottky diodes are employed as a nonlinear targets exhibiting strong second order harmonics. In an application involving the detection of asymmetric nonlinear targets like electronic devices, the presence of rusty and or cracked metals can increase the difficulty of identification. They can be distinguished from asymmetric targets, at least in part, by their symmetrical distortion and with stronger odd order harmonics

3. LITERATURE REVIEW

The work presented here employs TR techniques to detect, identify and focus energy on NL targets, specifically semiconductor junctions. The work in time-reversal originated in acoustics and continues to evolve with emerging applications, both in acoustics and in electromagnetics. This section serves to summarize the work of the investigators most involved in time-reversal and nonlinear detection.

Time-Reversal Mirror

Time-Reversal was introduced as an ultrasonic method for the detection and locating acoustic scatterers in inhomogeneous mediums by Mathias Fink. Time-reversal permits one to collect scattered waves and, due to the TR invariance of the wave equation, then reverse the propagation paths of these scattered waves to focus upon the point from which they originated [1]. Figure 3.1 illustrates the process for focusing on targets using a Time-Reversal Mirror (TRM).

As shown in Figure 3.1(a) an interrogation pulse is first transmitted from one of the elements in the array. The scattered response is then received at all elements in the array shown in Figure 3.1(b). These responses are then time reversed (also referred to as mirrored in the DORT research community) so that they focus at the target location as shown in Figure 3.1(c) [1]. The first challenge encountered by early workers was regarding how to treat the case when multiple targets are present. If two targets were present, for example, the original TR techniques could not selectively focus on each target, especially one target scattered more strongly than the other, which would often result in the target with the strongest scattered signal being focused upon most strongly. For many applications, one would like to selectively focus upon the target to receive the focused signal, a task for which the standard TRM is inadequate.

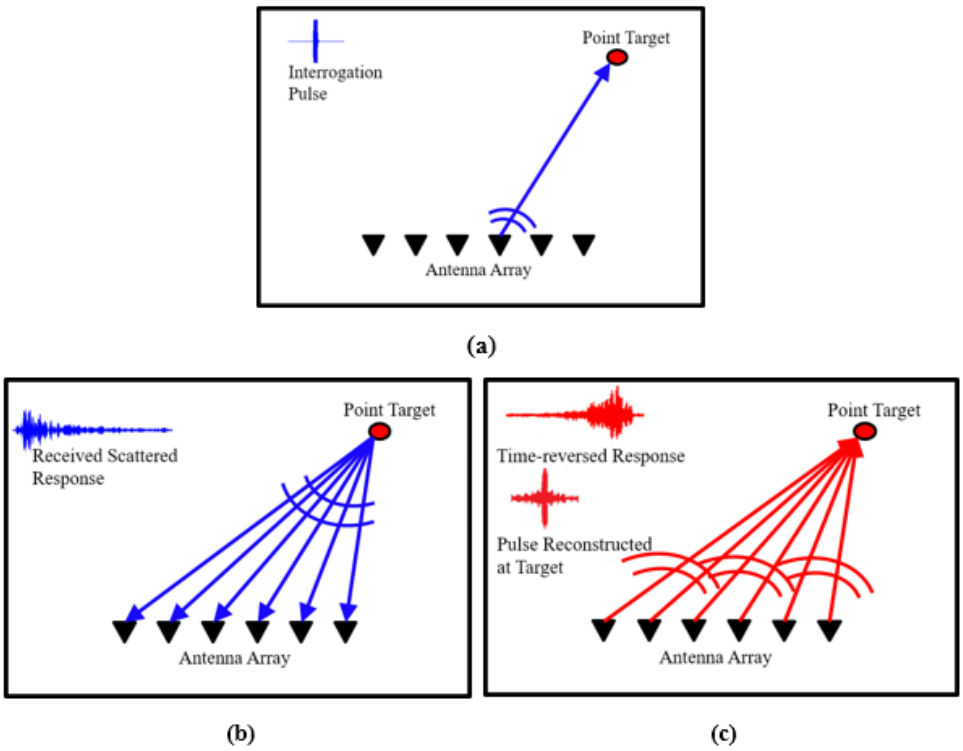

Figure 3.1: Illustration of the TRM process of focusing to a point scatterer (a) the environment is interrogated with a short pulse (b) the scattered response suggests a complex medium and (c) the signal is mirrored in time and re-transmitted to reconstruct the pulse at the target

The DORT Method

DORT is an adaptation of the TRM in which a multi-static matrix is decomposed into eigenvalues and eigenvectors. An NxN matrix is constructed from the multi-static data received from the transducer array. The matrix is then decomposed into eigenvalues and eigenvectors, where each nonzero eigenvalue represent a scatterer. The most dominant scatterer is represented by the first eigenvalue and the rest are in descending order. The eigenvectors correspond to the magnitudes and phases of the array elements necessary to focus on the corresponding scatterer or target. The DORT allows the beamforming information necessary to steer an array to multiple targets to be gleaned from the environment through interrogating the environment with the array. The DORT technique was first developed by Prada et al. and is executed by first having one

transducer (antenna) transmit a short pulse with a finite bandwidth. Next, the data is received by all transducers in the array. The data is rearranged into an NxN matrix for every sample in time $\boldsymbol{M}$ as shown in Figure 3.2(a).

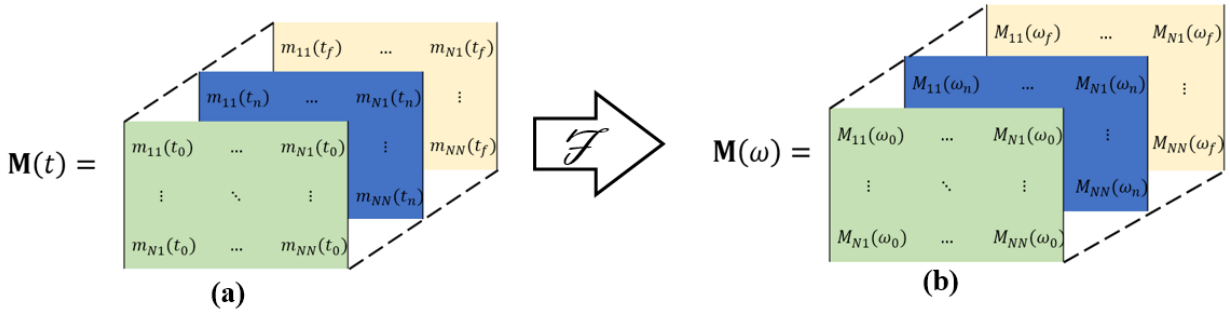

Figure 3.2: Multi-static data matrix in (a) time domain and (b) frequency domain

The transfer matrix $\boldsymbol{H}$ is used to better represent the frequency response of the targets and is obtained from the following expression:

$$\boldsymbol{M}(\omega) = f(\omega)\boldsymbol{H}(\omega) \tag{3.1}$$

$\boldsymbol{H}$ can be found using (3.1) where $f(\omega)$ is the frequency domain expression of the transmitted pulse. Next, the transfer matrix $\boldsymbol{H}$ can factored using Green's functions:

$$\boldsymbol{H}(\omega) = \boldsymbol{P}(\omega)\boldsymbol{S}(\omega)\boldsymbol{P}^{T}(\omega) \tag{3.2}$$

Where $\boldsymbol{P}(\omega) = [\boldsymbol{g}(\underline{\boldsymbol{r}}_1, \omega) \quad \boldsymbol{g}(\underline{\boldsymbol{r}}_2, \omega) \quad \ldots \quad \boldsymbol{g}(\underline{\boldsymbol{r}}_N, \omega)]$ is the propogation matrix where $\boldsymbol{g}$ is the Green's function between a particular target and the array elements. The diagonal elements of $\boldsymbol{S}(\omega)$ represents the real valued scattering strength of the target, also referred to as the radar cross section. If the targets are well resolved, such that there is no scattering between the targets, the off diagonal elements of $\boldsymbol{S}(\omega)$ are identically zero.

The time-reversal operator (TRO) is the separable matrix that is defined as:

$$\boldsymbol{T}(\omega) = \boldsymbol{H}^{\dagger}(\omega)\boldsymbol{H}(\omega) \tag{3.3}$$

The Hermitian conjugate of the transfer matrix represents time-reversal in the frequency domain. The TRO matrix $\boldsymbol{T}$ is a self-adjoint since it is the product of a matrix and its conjugate transpose. Therefore, the eigenvalue decomposition could be found by taking the singular value decomposition of $\boldsymbol{H}^{\dagger}(\omega)$ and $\boldsymbol{H}(\omega)$ where they can be expressed as the following:

$$\boldsymbol{H}(\omega) = \boldsymbol{U}(\omega)\boldsymbol{\Sigma}(\omega)\boldsymbol{V}^{\dagger}(\omega) \tag{3.4a}$$

$$\boldsymbol{H}^{\dagger}(\omega) = \boldsymbol{V}(\omega)\boldsymbol{\Sigma}^{\dagger}(\omega)\boldsymbol{U}^{\dagger}(\omega) \tag{3.4b}$$

$\boldsymbol{U}(\omega)$ and $\boldsymbol{V}(\omega)$ are unitary matrices $\boldsymbol{\Sigma}(\omega)$ are the real valued singular values $\boldsymbol{H}(\omega)$ of and Now putting (3.4a) and (3.4b) into (3.3):

$$\boldsymbol{T}(\omega) = \boldsymbol{V}(\omega)\boldsymbol{\Sigma}^{\dagger}(\omega)\boldsymbol{U}^{\dagger}(\omega)\boldsymbol{U}(\omega)\boldsymbol{\Sigma}(\omega)\boldsymbol{V}^{\dagger}(\omega) \tag{3.5}$$

Because $\boldsymbol{U}$ is unitary (3.5) can be written as:

$$\boldsymbol{T}(\omega) = \boldsymbol{V}(\omega)\boldsymbol{\Lambda}(\omega)\boldsymbol{V}^{\dagger}(\omega) \tag{3.6}$$

Where the matrix $\boldsymbol{\Lambda}(\omega) = \boldsymbol{\Sigma}^{\dagger}(\omega)\boldsymbol{\Sigma}(\omega)$ is a real valued diagonal matrix whose elements are the eigenvalues of the TRO matrix and the nonzero eigenvalues are representative of the resolved targets. Another graphic showing the structure of (3.7) is shown in Figure 3.3.

$$\mathbf{T}(\omega) = \begin{bmatrix} | & \dots & | \\ V_1(\omega) & \dots & V_N(\omega) \\ | & \dots & | \end{bmatrix} \begin{bmatrix} \Lambda_1(\omega) & 0 & 0 \\ 0 & \ddots & 0 \\ 0 & 0 & \Lambda_N(\omega) \end{bmatrix} \begin{bmatrix} - & V_1^*(\omega_0) & - \\ \vdots & \vdots & \vdots \\ - & V_1^*(\omega_0) & - \end{bmatrix}$$

Figure 3.3: Eigenvalue Decomposition of TRO Matrix

By substituting (3.2) into (3.3) the TRO matrix $\boldsymbol{T}$ can be expressed as:

$$\boldsymbol{T}(\omega) = \boldsymbol{P}^{*}(\omega)\left[\boldsymbol{S}^{\dagger}(\omega)\boldsymbol{P}^{\dagger}(\omega)\boldsymbol{P}(\omega)\boldsymbol{S}(\omega)\right]\boldsymbol{P}^{T}(\omega) \tag{3.7}$$

Wherein comparing (3.6) to (3.7) one can see that $\boldsymbol{\Lambda}(\omega) = \boldsymbol{S}^{\dagger}(\omega)\boldsymbol{P}^{\dagger}(\omega)\boldsymbol{P}(\omega)\boldsymbol{S}(\omega)$, $\boldsymbol{V}(\omega) = \boldsymbol{P}^{*}(\omega)$, and $\boldsymbol{V}^{\dagger}(\omega) = \boldsymbol{P}^{T}(\omega)$.

A function can be generated using the eigenvalue λ_i and associated eigenvector $\boldsymbol{v_i}$, which represents the phase conjugated (time-reversed) Green's function between the array elements and the i^{th} target, such that the focusing signal $\boldsymbol{k_i}$ can be expressed as:

$$\boldsymbol{k}_i(\omega) = \lambda_i(\omega)\boldsymbol{v}_i(\omega) \tag{3.8}$$

The focusing signal $\boldsymbol{k_i}$ can be found for each array element and when transmitted simultaneously the signal will be focused on the target [2] [5] [6].

Pulse Inversion

The targets of interest we consider here are nonlinear. Most electronic devices contain semiconductor junctions (e.g., diodes, transistors, etc.) and therefore exhibit harmonic responses upon excitation. The generated harmonics are difficult to distinguish since they can be orders of magnitude smaller than the fundamental of linear scatterers. The range of the scattered signal, including the large linear signals and much smaller NL ones, can exceed the dynamic range of most receivers, leading to linearity problems and so compromise the received data, rendering it useless and thus making it impossible to discern nonlinear scatterers from linear scatterers. Receivers are typically tuned to receive a range of power from the minimum receive power or sensitivity, known as the minimum discernable signal (MDS). The dynamic range (DNR) is defined by the largest signal that the receiver can see before the receiver amplifier begins to saturate causing nonlinear distortion.

Leighton discussed suppressing clutter and improving target discrimination by employing twin inverted pulses as an excitation [7]. The respective scattered signals from this excitation are

then combined at the receiver. Once combined, the odd ordered harmonics are canceled out, and the even-ordered harmonics are enhanced, allowing additional information to be acquired for small NL targets. As this technique is further developed and refined, one can imagine gathering a variety of important date – e.g., device type, possible function, identification.

Pulse inversion is done by using two transmit pulses similar to those shown in Figure 3.9, namely $p(t)$ and $n(t)$, where $n(t) = -p(t)$. The received signals for each pulse can be expressed as the power series expansion below:

$$k^{+}(t) = k_1 p(t) + k_2 p^2(t) + k_3 p^3(t) \ldots \quad (3.9a)$$

$$k^{-}(t) = -k_1 p(t) + k_2 p^2(t) - k_3 p^3(t) \ldots \quad (3.9b)$$

It is obvious that the linear combination of $k^{+}(t)$ and $k^{-}(t)$ will numerically eliminate the odd-ordered harmonics and enhance the even-ordered harmonics by a factor of two.

$$k^{+}(t) + k^{-}(t) = 2k_2 p^2(t) + 2k_4 p^4(t) \ldots \quad (3.10)$$

With the fundamental and odd ordered harmonics suppressed, the detection of electronic devices becomes a much easier problem. The effects of all linear scatterers are mitigated, and nonlinear objects that are not of interest such as rusty or cracked metal are also mitigated since they tend to only exhibit third order harmonics [7].

Nonlinear Time-Reversal

Since the wave equation is the governing relationship for both electromagnetic waves and acoustic waves because they are both transverse waves, the scattering phenomena in both fields are similar, and most ultrasound techniques can be applied to electromagnetic radar. In Hong et al. pulse inversion and time-reversal were combined and applied to electromagnetic waves [8]. The purpose of the experiment was to demonstrate that time-reversal combined with pulse inversion

would serve as a good technique for detecting and locating electronic devices in a complex environment, resembling a room with windows, from the outside.

The experiment was set up to use a bi-static system to detect a nonlinear target in a reverberant chamber. The reverberant chamber had openings that could represent windows in a building and a stirrer to make a chaotic wave propagation environment. A TRM typically requires that an array of transducers be surrounding the target; however, since the environment is wave chaotic, it is suitable to perform time-reversal using a single antenna.

In a chaotic wave propagating environment, Hong et al. demonstrated that TR could be an effective technique for focusing electromagnetic waves to NL targets [8]. The work demonstrates nonlinear time-reversal and pulse inversion in electromagnetics and sets the foundation and motivation for the rest of the work demonstrated in this thesis.

4. SIMULATED PI-DORT

The DORT method combined with PI was validated in simulation. Two cases were investigated for simulation: the first configuration is with 1L target and 1NL target, and the second configuration is with two NL targets. The results were published and presented at URSI GASS 2017 in Montreal, QC, Canada.

Method

To simulate the proposed approach, a quasi-2D electromagnetic model was generated in CST Microwave Studio. Two parallel PEC boundaries separated by 1 cm are placed in the z-axis. Since the separation between the PEC boundaries are much smaller than the wavelength, the model effectively represents a 2D space where the electric field is perpendicular to the *x*-*y* plane and propagate only in the *x* and *y* directions. A 12-element point source array was used with an element spacing of 7.5 cm (Figure 4.1). The incident pulse used in the simulation was a modulated Gaussian pulse centered at 1.25 GHz with a bandwidth of 0.5 GHz.

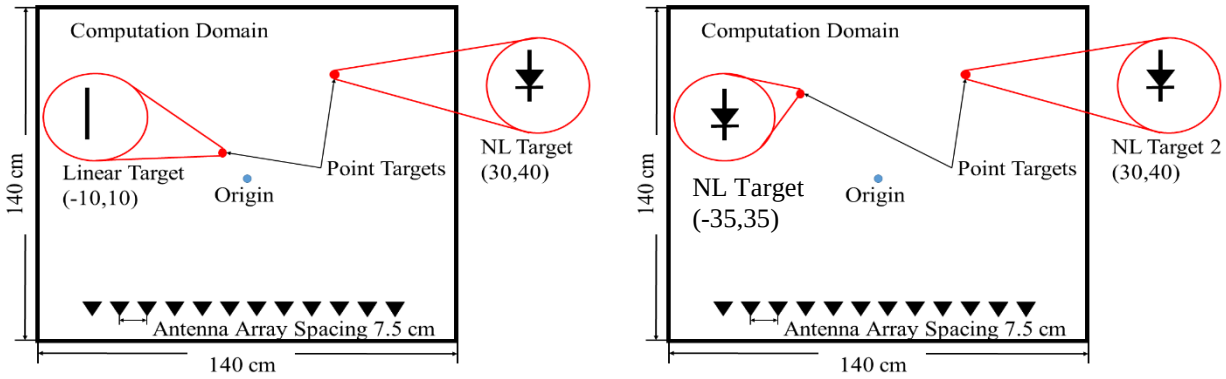

Figure 4.1: PI-DORT simulation domain (a) first configuration with one linear and one nonlinear target (b) second configuration with two nonlinear targets

The first configuration includes two point targets as shown in Figure 4.1(a). One target is a linear scatterer represented by a short circuit (thin wire) connecting the top and bottom PEC boundaries, and the other is an NL target represented by a diode. For this simulation, DORT was applied to two different sets of data. The first data is the multi-static response using a positive pulse $p(t)$ after background subtraction, where the background is the same environment with the targets removed, to remove inter-element coupling. The second set is the multi-static data after applying PI to eliminate fundamental (including inter-element coupling) and odd-order harmonics.

The second configuration consists of two nonlinear targets (also represented by diodes) as shown in Figure 4.1(b). DORT was applied after PI for selective focusing on each target using the second harmonic frequency.

Results

The results for the first configuration and second configuration (Figure 4.1(a) and Figure 4.1(b) respectively) demonstrate the separation between eigenvalues for well-resolved scatterers. The figures of merit include eigenvalues and 2D E-Field heat maps for focusing simulations.

One Linear and One Nonlinear

Figure 4.2 shows the eigenvalues of TRO from the first configuration (1L and 1NL target) after background subtraction. Two significant eigenvalues are obtained, one representing the nonlinear scatterer and the other representing the linear scatterer. It is shown that only one of the eigenvalues, λ_1, has significant amplitudes in the harmonic bands.

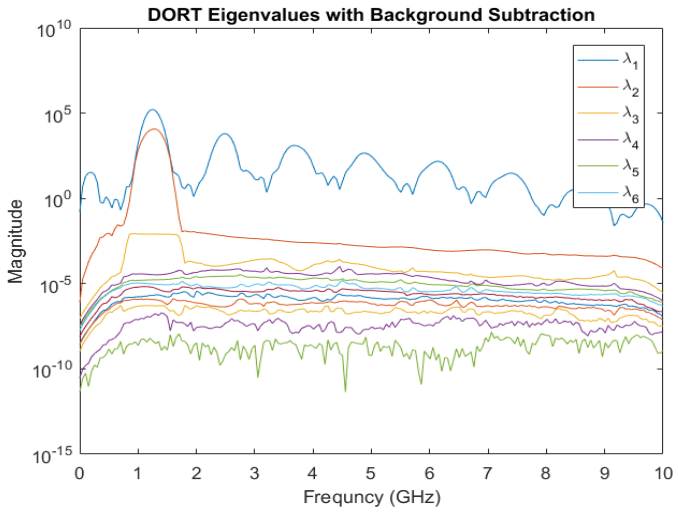

Figure 4.2: DORT using background subtraction for 1L and 1NL target

The eigenvectors associated with λ_1 and λ_2 at the fundamental center frequency (1.25 GHz) were used to generate modulated Gaussian pulses to feed the array. Two separate focusing simulations were run for λ_1 and λ_2 and the results are shown in Figure 4.3(a) and Figure 4.3(b), respectively.

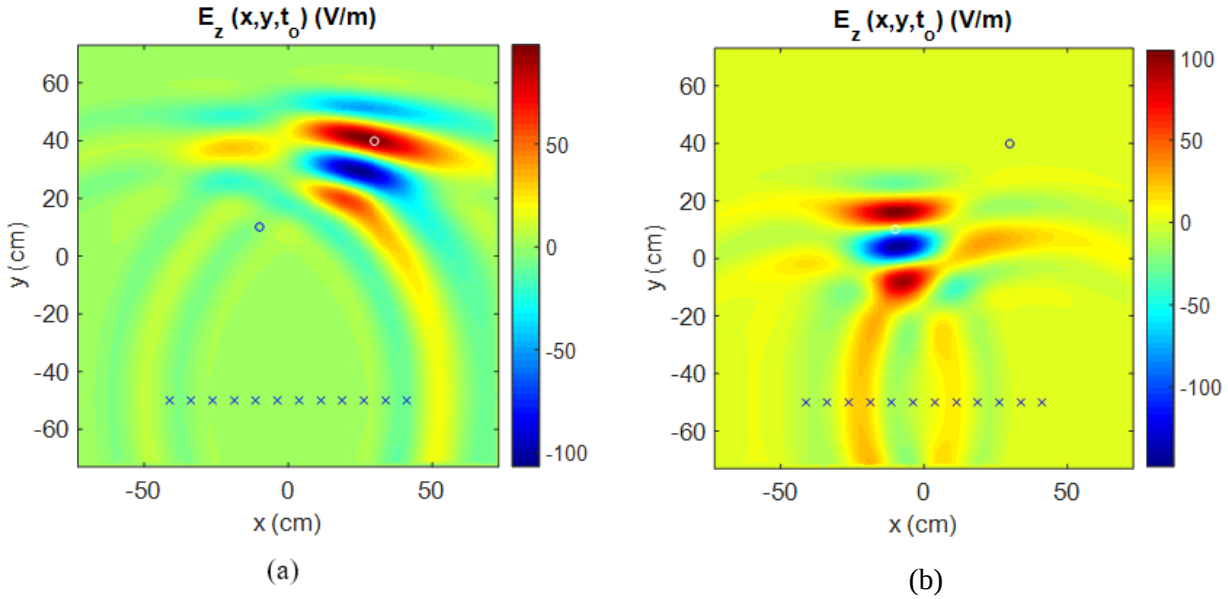

Figure 4.3: Simulated focusing results for (a) the first eigenvalue (λ_1) and (b) the second eigenvalue (λ_2)

Even though λ_1 is the one with significant amplitude at harmonic bands, the waves generated based on λ_1 seem to focus at the linear target (Figure 4.3(a)) and the waves generated based on λ_2 focus at the nonlinear target, indicating the eigenvalues were mixed up. One possible explanation is that, since eigenvalue decomposition (EVD) is done at each single frequency point without any information of EVD at other frequencies, the eigenvalues are obtained depending on the strongest scatterer at each frequency point. In other words, at the fundamental frequency band, the strongest scatterer is the linear scatter, and therefore it appears in the first eigenvalue. However at the harmonic frequencies, the nonlinear scatter is obviously the strongest scatterer and thus it appears in the first eigenvalue.

Figure 4.4 shows the eigenvalues of TRO from the first configuration after PI (PI-DORT). The fundamental and odd-order harmonics are minimized, making background subtraction unnecessary and eliminating the mix-up of the eigenvalues since the only dominant eigenvalue is over the even-order harmonic bands.

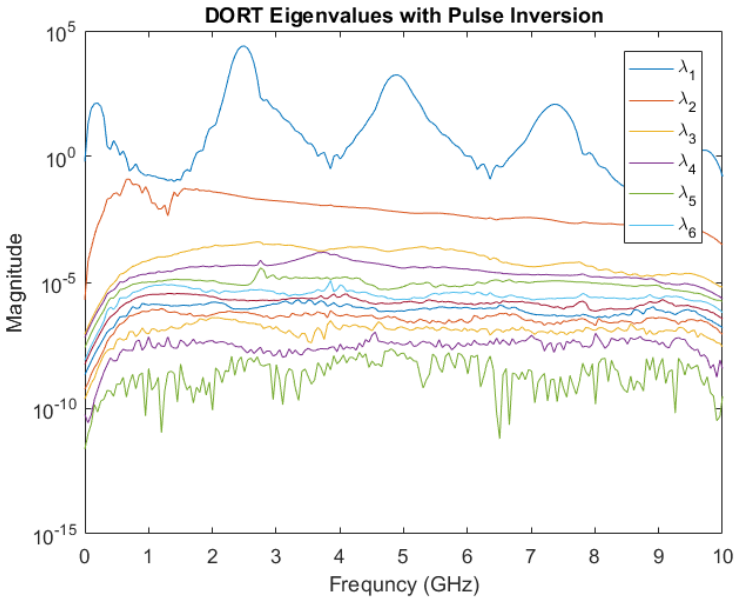

Figure 4.4: PI-DORT eigenvalues for 1L and 1NL target

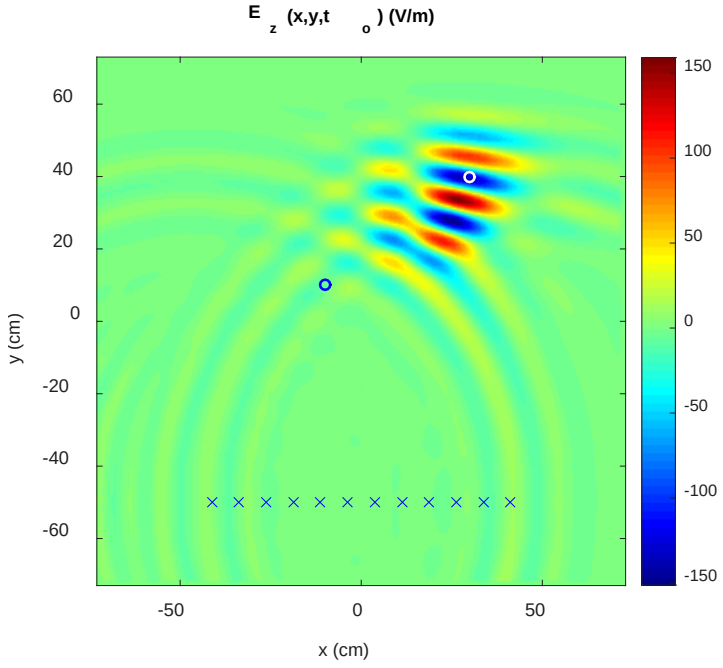

Figure 4.5: PI-DORT focusing onto 1NL target

Figure 4.5 shows the results of focusing on a nonlinear target when the eigenvectors associated with λ_1 at the second harmonic frequency (2.5 GHz) were used to generate modulated Gaussian pulses to feed the array. The focusing occurs at the nonlinear target as expected.

Two Nonlinear

Figure 4.6 shows the eigenvalues of TRO for the second configuration (Figure 4.1(b)) after applying PI-DORT. The fundamental and odd-order harmonics are also eliminated in this case, but two significant eigenvalues appear at even-harmonic bands since there are two nonlinear targets.

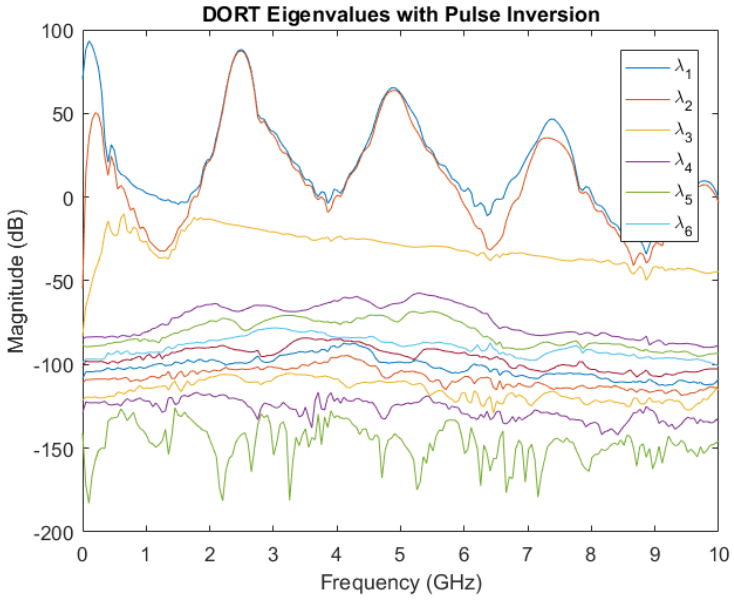

Figure 4.6: Eigenvalues for 2NL targets

Focusing simulations were run based on the eigenvector for λ_1 and λ_2, and the results are shown in Figure 4.7(a) and Figure 4.7(b), respectively. Each element was fed with phase shifted Gaussian modulated monochromatic pulses at the peak of the 2nd-order harmonics 2.5GHz. As expected, each simulation shows wave focusing at each nonlinear element.

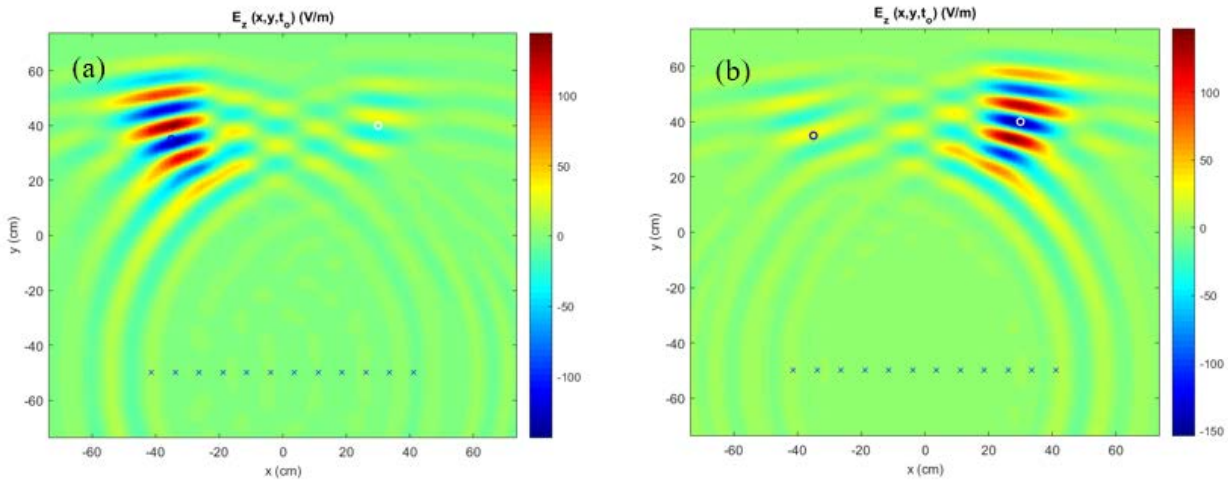

Figure 4.7: Focusing for 2NL targets with (a) eigenvalue 1 and (b) eigenvalue 2

Discussion

The simulated results verify the proposed technique of combining DORT with pulse-inversion to selectively focus energy to NL targets via harmonic detection. The cases demonstrate the technique applied to two cases: the first configuration (one linear target and one nonlinear target) and the second configuration (two nonlinear targets).

In the results of the case of one linear and one NL target, eigenvalue mixing is observed where the eigenvector at the fundamental frequency (1.25 GHz) associated with $\lambda_1$is observed to focus towards the linear target, and at the second harmonic (2.5 GHz) it is observed that the first eigenvalue focus to the NL target. One likely explanation of this is that in the singular value decomposition of the Hermitian conjugate of the transfer matrix the singular values are placed in descending order. At the fundamental frequency the linear target is the strongest scatterer, thus the corresponding eigenvector and eigenvalue appear at the first eigenvalue. Whereas the second order harmonic the only response is from the NL scatterer. This phenomeon will be addressed in the future work.

5. DESCRIPTION OF MODEL

The section of this thesis serves to describe the individual components of the experimental set up including the experimental procedure. This section is provided for readers who wish to learn more detail about the development of the testbed. This section may be skipped and there would still be continuity. However, for a more comprehensive description of the chronological testbed development the reader is urged to continue.

Vivaldi Antenna

Conventional technology for broadcast and communications utilize narrowband signals to transmit data. There is interest amongst researchers using ultra-wideband (UWB) signals for communications, imaging, radar, etc. UWB offers advantages over electromagnetic compatibility over other systems. The power spectrum is dispersed over a large range of frequencies such that no piece of the spectrum penetrates above the noise floor. Because of this, UWB signals can coexist with conventional narrowband broadcast signals without interfering with them and are also more immune to interference from them.

A Vivaldi antenna is an exponentially tapered slot antenna which is often used for UWB radar and imaging applications because of its broadband performance and good directionality. As illustrated in Figure 5.1, an electric field develops a curvature as the wave transitions from the antenna to free space, a bowing which limits the gain or directionality of the antenna. As an aside, a related investigation on the use of spatially-variant electromagnetic materials to further improve the Vivaldi's directivity is reported in Appendix C of this thesis.

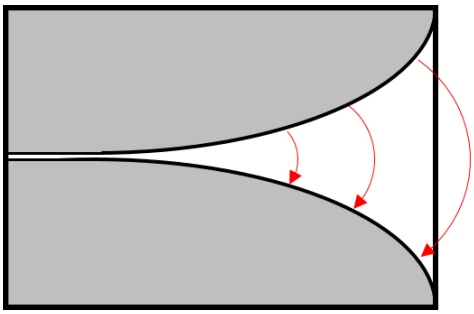

Figure 5.1: Electric Field lines on a Vivaldi antenna

The antenna designed for this experiment is an antipodal variation of the Vivaldi antenna where two exponentially tapered conductor flares separated by a dielectric are fed with a microstrip transmission line.

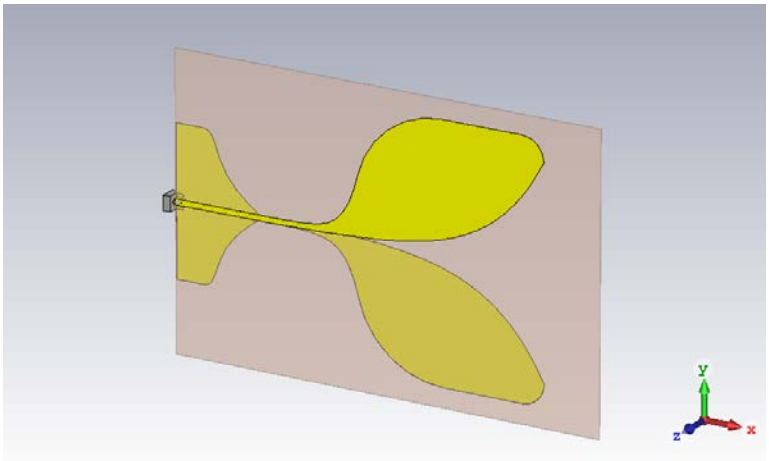

Figure 5.2: CST Model of Vivaldi Antenna

The radiating bandwidth of the antenna is commonly held as those frequencies where the return loss is less than -10dB, shows a bandwidth which spans from 1.1GHz to 20 GHz as shown in Figure 5.3.

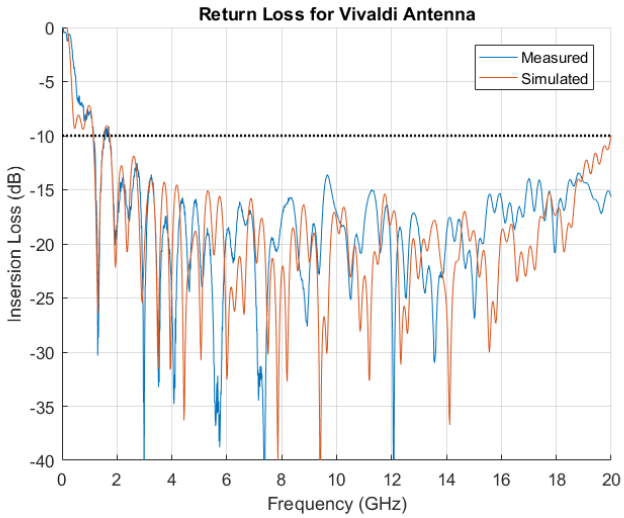

Figure 5.3: Measured and Simulated Return Loss for two Vivaldi antennas

A useful figure of merit for the antenna is the usable gain bandwidth. We are interested in the antenna's radiation in the direction of the targets. It is desired that the antenna to have a realized gain of greater than 10 dB in the direction of propagation over the operating frequency, which will henceforth be known as the usable gain bandwidth. To measure this a pair of antennas were placed in the far-field of each other, and the transmission was measured using a vector network analyzer (VNA) as shown in Figure 5.4.

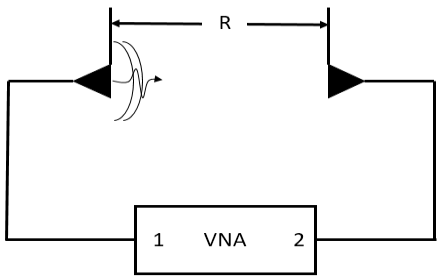

Figure 5.4: Usable Gain Bandwidth measurement setup

Using the Friis transmission equation (5.1) the realized gain, including reflection loss, is extracted and compared to simulation.

$$\frac{P_r}{P_t} = G^2\left(\frac{\lambda}{4\pi R}\right)^2 \tag{5.1a}$$

$$G = \left(\frac{4\pi R}{\lambda}\right)\sqrt{S_{21}}, \quad S_{21} = \frac{P_r}{P_t} \tag{5.1b}$$

The realized gain vs. frequency in Figure 5.5 shows a usable bandwidth spanning from 3 to 12 GHz.

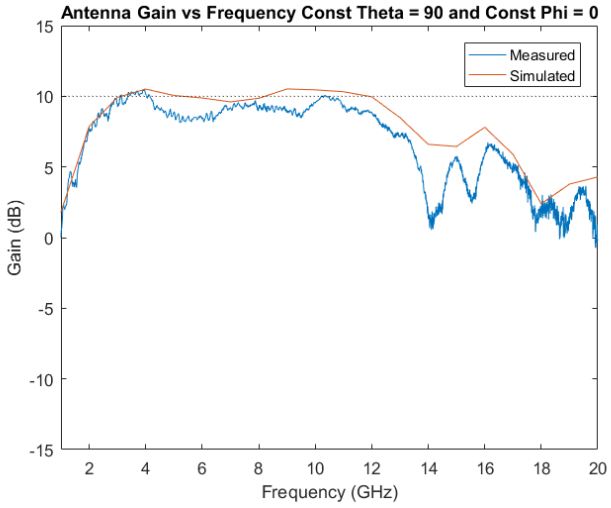

Figure 5.5: Usable Gain Bandwidth for Vivaldi antennas

Antenna Array

Array spacing is a critical parameter which determines the sampling angle for spatial sampling of the environment. A widely spaced array, or more commonly known as a distributed antenna network, can have significant spatial sampling. However, the focusing of a distributed antenna network tends to introduce grating lobes resulting in less focusing. As the array spacing decreases, the angle of spatial resolution increases. Consider Figure 5.6; the point target is assumed to be in the far-field for the array such that the Fraunhofer approximation can be applied.

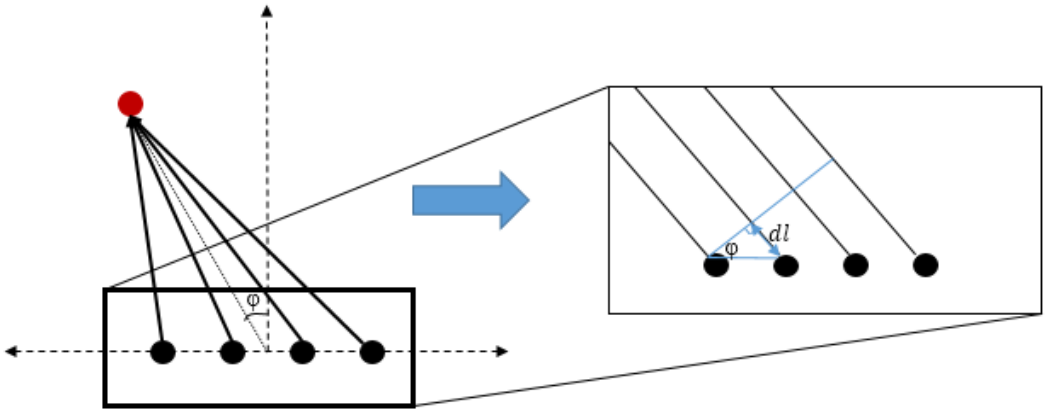

Figure 5.6: Illustration of the Fraunhofer approximation in an array

Using the Fraunhofer approximation, one can infer the angle at which the target is located off the normal of the broadside of the array is the same for each element in the array, and can be approximated so that:

$$\Delta l = d \sin \Delta\varphi \tag{5.2}$$

The differential length, Δl, is limited by the sampling rate of the receiver and can be expressed as the following:

$$\Delta l = \Delta t \cdot c \tag{5.3}$$

Where (Δt) is the minimum time-step of the receiver and (c) is the speed of propogation in free space. By substituting (5.3) into (5.2) and solving for ($\Delta\varphi$):

$$\Delta t \cdot c = d \sin \Delta\varphi \tag{5.4a}$$

$$\Delta\varphi = \sin^{-1} \frac{4\Delta t \cdot c}{d} \tag{5.4b}$$

Distributed Antenna Network

In a distributed antenna network the target is assumed to be in the far-field for each antenna element but not for the entire array – DORT does not require the target to be in the far-field of the array. A large antenna spacing reduces the effect of inter-element coupling which can make measurements difficult by exceeding the dynamic range of the receiver since the signals given by inter-element coupling can have a magnitude much larger than the expected response from a target.

Another advantage to a distributed antenna network is that there is a greater spatial resolution because the path length between elements is greater in a distributed network than a tight array.

Linear Target

The first DORT measurements were taken with linear targets to simplify measurements as the testbed was developed and refined. Measurements from the multi-static array were taken with a metallic sphere placed in the center of the array cross-range and at 1.5 meters in down-range shown in Figure 5.7.

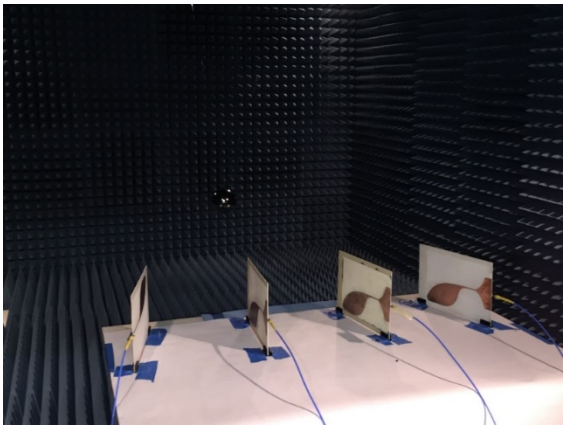

Figure 5.7: Metal sphere suspended in interrogation environment

The sphere was modeled in CST Microwave Studio® (CST MWS) with a plane wave excitation to determine its scattering pattern in Figure 5.8.

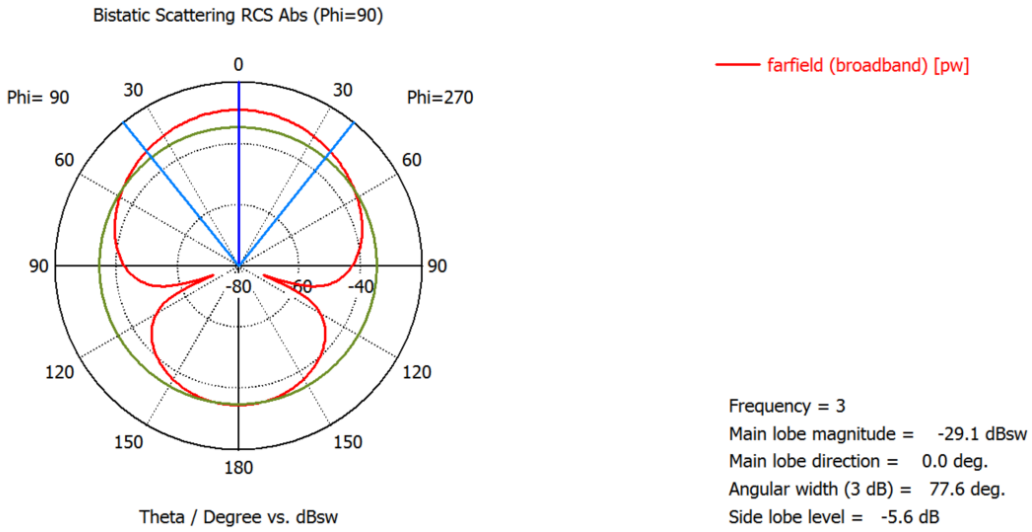

Figure 5.8: Simulated RCS pattern of a PEC sphere

Nonlinear Target

As shown in Figure 5.9, Schottky diodes made by Broadcom (HSMS2860) are placed at the feed points of broadband bowtie antennas to serve as NL targets. The bowtie antenna was fabricated on 1.02 mm thick Rodgers substrate (RO4730) with a relative permittivity of 3.

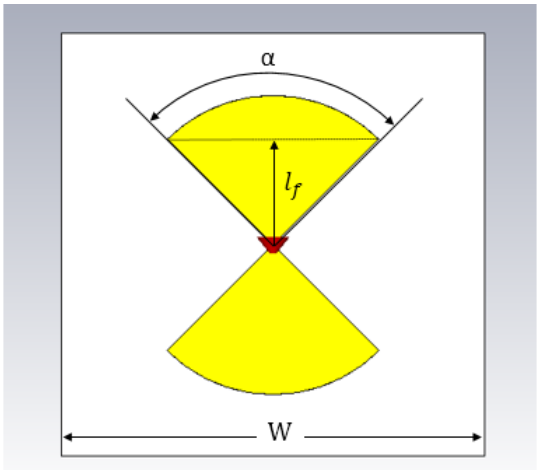

Figure 5.9: Bowtie antenna for NL targets

An important parameter to look at is the scattered signal (at 3 GHz) and radiation (at 6 GHz) pattern shown in Figure 5.10 given by a plane wave excitation. This is important because RCS is directly related to the power received by the diode which needs to be large enough to generate harmonics.

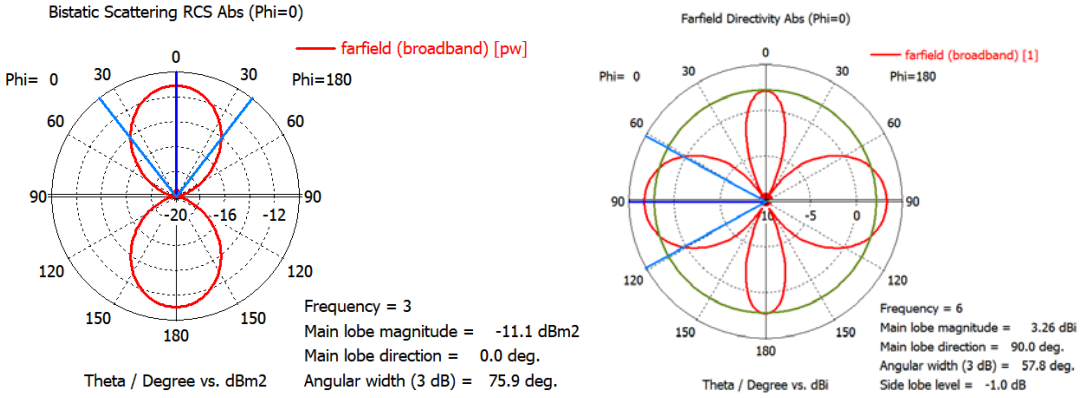

(a) (b)

Figure 5.10: Bowtie Antenna for NL Targets (a) Scattering Pattern at 3 GHz and (b) radiation pattern at 6 GHz

Interrogation Pulse

The pulsed used in simulation and experimentation is a sinusoidal modulated Gaussian pulse with a bandwidth of 2 GHz centered at 3 GHz. The time domain and frequency domain representation of the pulse is shown in Figure 5.11.

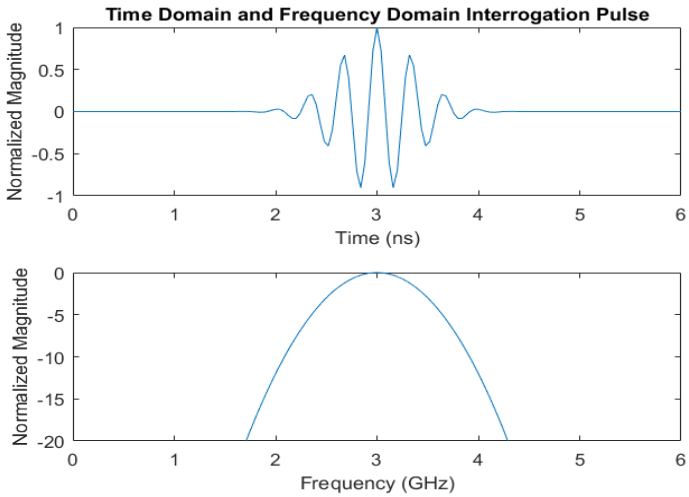

Figure 5.11: Interrogation Pulse

DORT Processing Script

To process the experimental data, the DORT time-domain multi-static dataset which includes the mono-static and bi-static responses, is input into the DORT Matlab script (provided in Appendix B). The code first extracts the time-domain data from each measurement and places it into a matrix with rows equal to the number of time samples and columns equal to the number of elements in the array squared. For example, an experimental set up with a four-element array will appear as the following.

$$\begin{array}{|c|c|c|c|} \hline m_{11} \dots m_{41}(t_0) & m_{12} \dots m_{42}(t_0) & m_{13} \dots m_{43}(t_0) & m_{14} \dots m_{44}(t_0) \\ \vdots & \vdots & \vdots & \vdots \\ m_{11} \dots m_{41}(t_f) & m_{12} \dots m_{42}(t_f) & m_{13} \dots m_{43}(t_f) & m_{14} \dots m_{44}(t_f) \\ \hline \end{array}$$

Figure 5.12: Data Import matrix in the time-domain

The matrix shown in Figure 5.12 is broken up into 4 sections where each section represents a column in the multi-static matrix, that is that each section is broken up by the data sets provided by the transmit antenna. In the figure above the blue section contains all the data where antenna 1 is the transmit antenna, the green section where antenna two is the transmit antenna, the beige section where antenna 3 is the transmit antenna, and finally orange section where antenna four is the transmit antenna. The matrix is then transferred to the frequency domain by means of Fourier transform Figure 5.13.

$$\begin{array}{|c|c|c|c|} \hline m_{11} \dots m_{41}(\omega_0) & m_{12} \dots m_{42}(\omega_0) & m_{13} \dots m_{43}(\omega_0) & m_{14} \dots m_{44}(\omega_0) \\ \vdots & \vdots & \vdots & \vdots \\ m_{11} \dots m_{41}(\omega_f) & m_{12} \dots m_{42}(\omega_f) & m_{13} \dots m_{43}(\omega_f) & m_{14} \dots m_{44}(\omega_f) \\ \hline \end{array}$$

Figure 5.13: Data-Import matrix in the frequency domain

This data can be portrayed in three dimensions and arranged in four frames where each frame is mapped to one of the sections shown in the matrix above.

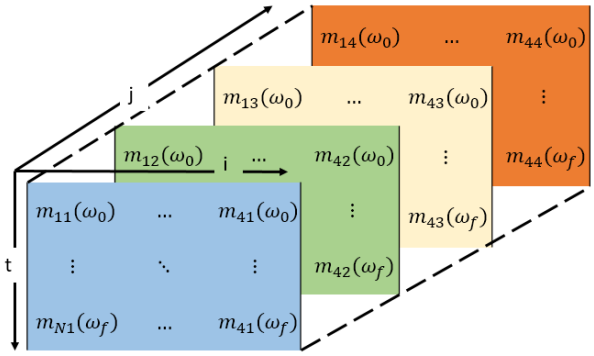

Figure 5.14: multi-static matrix unarranged

Notice the coordinates of the matrix above (Figure 5.14), the matrix has the coordinates $t \times j \times i$ and DORT works with the matrix $i \times j \times t$. A simple permute function in Matlab allows us to change the order of the dimensions of any matrix so the data can be rearrange like the following (Figure 5.15 same figure as Figure 3.2) which is the matrix that can be used for DORT processing.

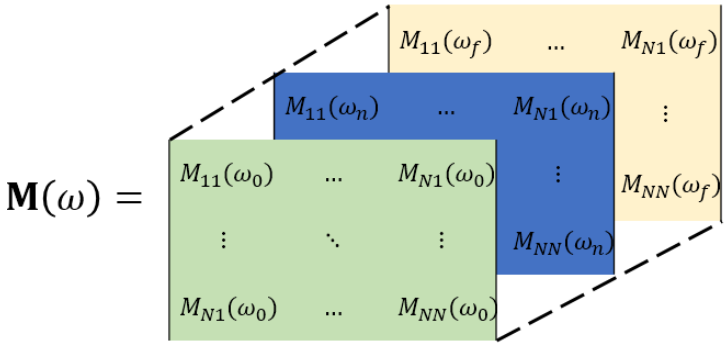

Figure 5.15: Multi-static data matrix in time domain

Experimental Procedure

The workflow for completing the DORT signal processing is shown in Figure 5.16. The workflow can be broken up into three distinct stages – interrogation, identification and transmission.

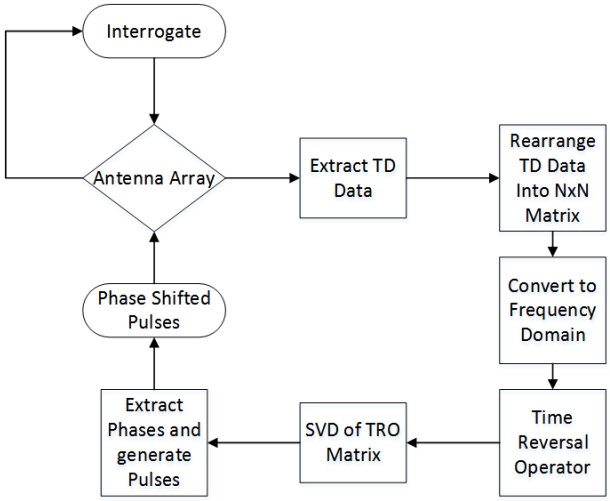

Figure 5.16: Workflow diagram for DORT experiment

The environment is illuminated with a short UWB pulse from an antenna array. Time domain data is extracted from simulation or oscilloscope. The data is then processed in Matlab, where the data is arranged into a multi-static $N \times N$ matrix (N is the number of array elements) and transformed into the frequency domain. Then we employ the time-reversal operator (TRO) and take the single-value decomposition (SVD) of the matrix. The entire band of eigenvalues and eigenvectors are used to generate TR pulses for UWB focusing to overcome multipath and complex environments. A more simplistic approach is using a monochromatic signals when there is line-of-sight of the target to the array a set of phase shifted sinusoidal waveforms are generated with the phase of the eigenvectors associated with the frequency. The sinusoidal waveform is then

truncated with a Gaussian window. In simulation the waveforms are Gaussian-windowed monochromatic signals.

The Testbed for the validation of DORT combined with PI is broken up into three parts, the computer (signal processing), the instrumentation, and the environment. Signal processing is exclusively performed using Matlab (see Appendix B). The instrumentation utilizes the available benchtop equipment including a 12.5 GHz dual-channel arbitrary waveform generator (AWG70002A), a 2-20 GHz power amplifier (RM20220), and a 12.5 GHz high-speed oscilloscope (MSO71254C).

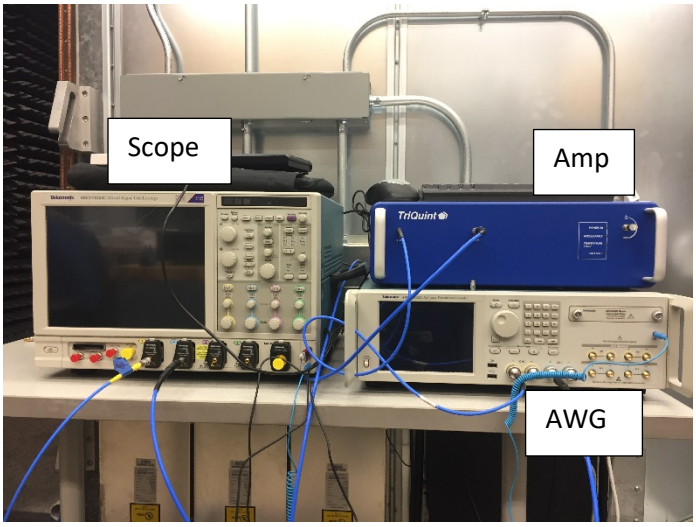

Figure 5.17: Benchtop Instrumentation for Experiment

The first step in DORT is the interrogation of the environment using a short pulse distinguishable in time. A pulse generated from Matlab (see Appendix A) is fed into the Tektronix AWG. The AWG has two channels 1 and 2 with two differential ports as shown in Figure 5.17. Channel 1 is amplified by the broadband amplifier which is then fed to the radiating antenna input.

Channel 2 will emit another pulse, delayed by 30ns to trigger the oscilloscope so that it can collect the scattered pulse return.

The output of channel 1 on the AWG feeds the input to an RF amplifier which provides 40dB of gain. The amplified pulse is then transmitted by a Vivaldi antenna. It is important that the Vivaldi antenna is facing the target in this experiment. This experiment power constrained which creates difficulty in exciting the nonlinearities of the diode. Therefore, to overcome path loss, the antennas need to have a high directivity to deliver maximum power to the diode.

The first case considered in this experiment was using a metallic sphere, similar to that of an RCS calibration sphere, to represent a linear target. Originally our antenna array spacing was 5 cm which was at the maximum spacing of $\frac{\lambda}{2}$ where $\lambda = 10\ cm$ before grating lobes would be seen in focusing. Grating lobes are when maxima occur where it is unexpected because the spacing of the array are greater than $\frac{\lambda}{2}$ such that maxima are repeated at unintended degrees of theta. This can be demonstrated via simulation. Consider an array of $\frac{\lambda}{2}$-length dipole antnnas. The target frequency is 3 GHz and $\lambda = 10\ cm$. In Figure 5.18(a) the spacing is 10 cm and in Figure 5.18(b) the spacing is 5 cm.

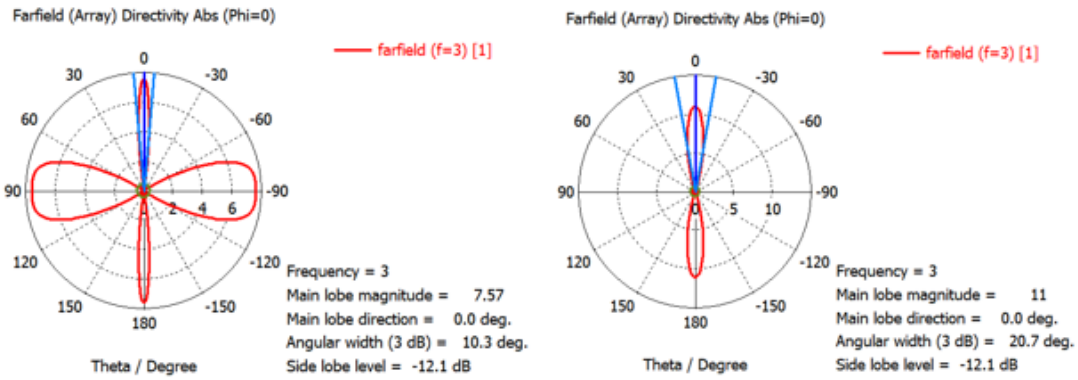

Figure 5.18: Demonstration of grating lobes with spacing (a) at 10 cm and (b) at 5 cm

The spacing 10 cm creates significant grating lobes at angles at theta equal to +/– 90 degrees, whereas no grating lobes exist with a spacing of 5 cm.

Figure 5.19 shows the initial test set-up. The sphere was placed 1.5 meters in down-range from the array with an element-spacing of 5cm with 6 elements. The array measurements were taken in a series of discrete measurements involving two antennas at a time by fixing the transmit antenna and changing the position of the receive antenna. After the first column of the multi-static matrix is filled, i.e., the receive antenna has been moved to each position, the position of the transmit antenna is changed, so the measurements for the next column of the multi-static matrix is acquired. This process is repeated for each column in the multi-static matrix. The sphere is then removed, and the measurements are repeated to obtain a background which will be used later to de-embed effects of inter-element coupling.

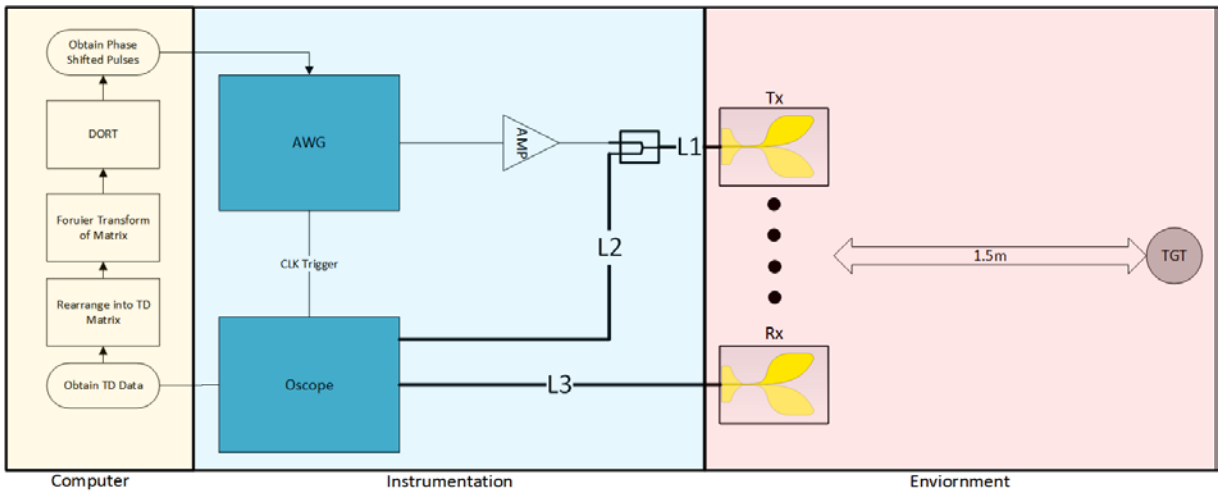

Figure 5.19: Initial Experimental Setup

Next, the signals are processed using the DORT code (Appendix B) which was verified by simulation. The initial results are shown below in Figure 5.20.

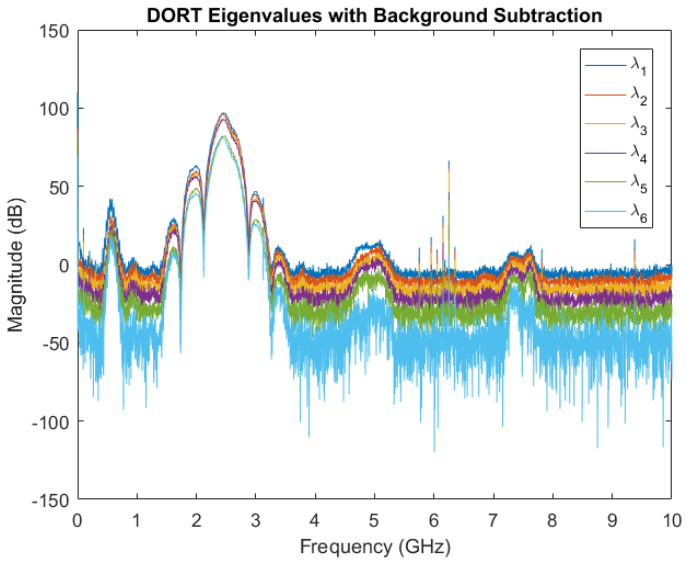

Figure 5.20: Initial DORT results: one linear target

There are several things in this figure that are not desirable. First, there is no significant separation of eigenvalues. Since there is only one target in the field, there should only be one non-zero eigenvalue ideally. Next, it is seen that there are harmonics at every integer multiple of 2.5 GHz which, for this case, was the center frequency of the transmit pulse. And there is also an unexpected signal at 500 MHz.

The first thing investigated was the separation issue. At this time the harmonics generated were not the primary concern since this could be explained by nonlinearities in the oscilloscope or amplifier. It was determined that the antenna coupling was affecting our ability to resolve the target, that a relatively large amount of energy was being coupled directly between antenna elements, creating difficulties in correctly processing the smaller signals from the target. Looking at some time-domain data shown in Figure 5.21.

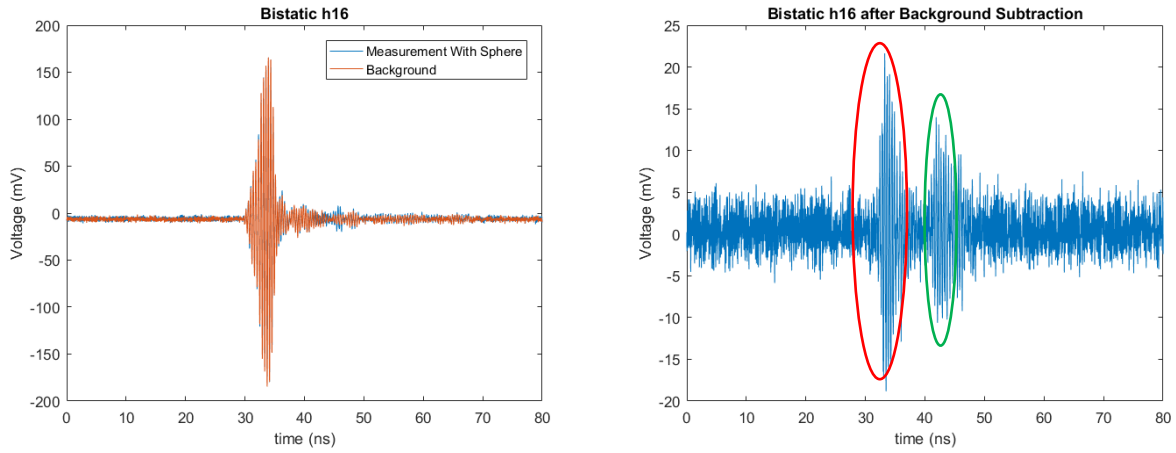

Figure 5.21: Initial bi-static result one linear target (a) raw measurement (b) background subtracted

In Figure 5.21(a) the raw measurement for a single bi-static measurement (m_{16}) is plotted. One trace is with the sphere, and one is without the sphere. While it is visible, one can see there is little difference in the two traces. At around 45ns the trace with the sphere (blue) peaks out from behind the background measurement (orange). Next, we subtract the background from the trace with the sphere, and the resulting plot is shown in Figure 5.21(b) even though the background is subtracted out there is some quantization noise that is so great that the subtracted "error" is greater than the signal we are trying to see. The antenna coupling (circled in red) is thought to be the pulse circled in red because the difference in time that the two pulses arrive (green minus red) is around 10ns which is the expected time of arrival. For a 3 meter (1.5 * 2) path length at $3 \times 10^8 \ {}^{m}/_{s}$ for propagation velocity, the time expected time of arrival is 10 ns. So it can be inferred that the pulse circled in red represents the inter-element coupling subtraction error and the pulse circled in green represents the scattered response from the metal sphere. Another difficulty encountered was that it appeared that the pulses received by each bi-static measurement were arriving at the same time because the time difference was smaller than the oscilloscope sampling rate as explained below. When considering the path length difference we had the following shown in Figure 5.22.

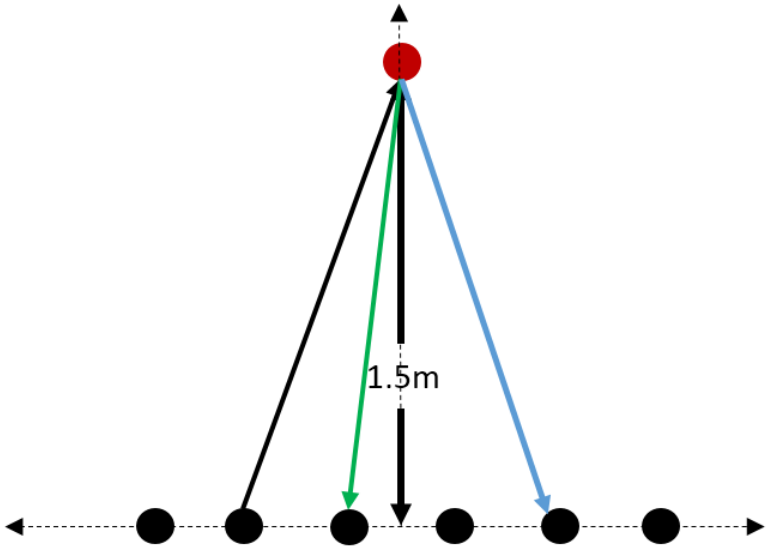

Figure 5.22: Relative path length differences

The relative path length difference between the green path and the blue path can be calculated as follows:

$$\Delta l = \sqrt{0.025^2 + 1.5^2} - \sqrt{0.075^2 + 1.5^2}$$

$$\Delta l = 1.7 \times 10^{-3} m$$

Relating the relative path difference to time we get:

$$t = \frac{\Delta l}{c}$$

$$t = (1.7 \times 10^{-3})/(3 \times 10^{-8})$$

$$t = 5.5\ ps$$

The expected time between each pulse is 5.5 ps which is much less than the sampling rate of the scope (20 ps/sample). Therefore the oscilloscope could not possibly distinguish the arrival time for each path. This same limitation was also the possible source of the difficulty in separating the eigenvalues.

To address this challenge, the antenna array was spaced out which gives a larger path length difference that can be resolved by the oscilloscope as well as having the added benefit of reducing inter-element coupling. The new test set up is shown below in Figure 5.23.

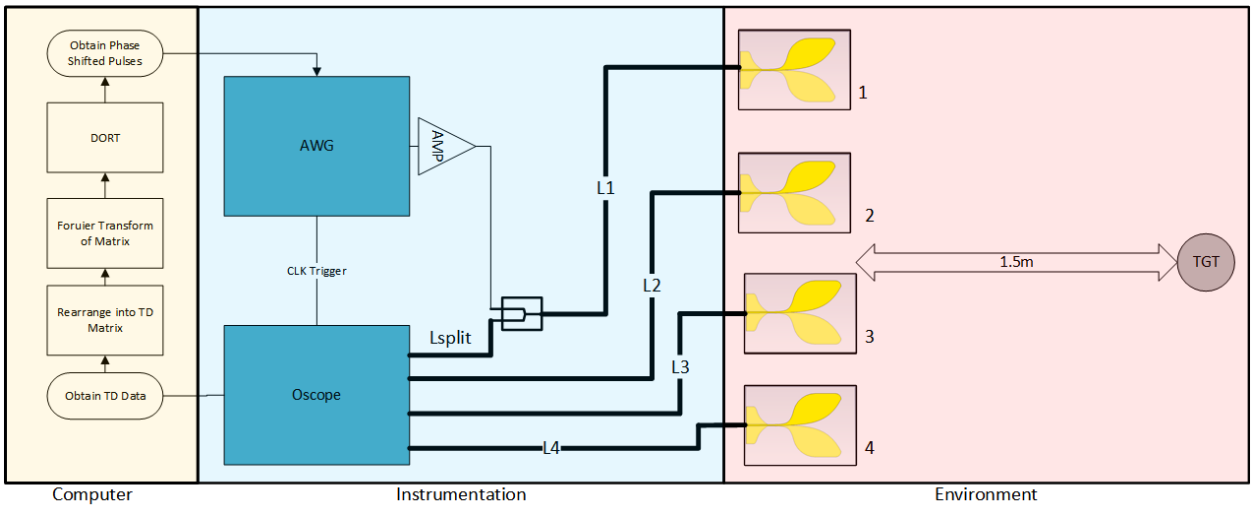

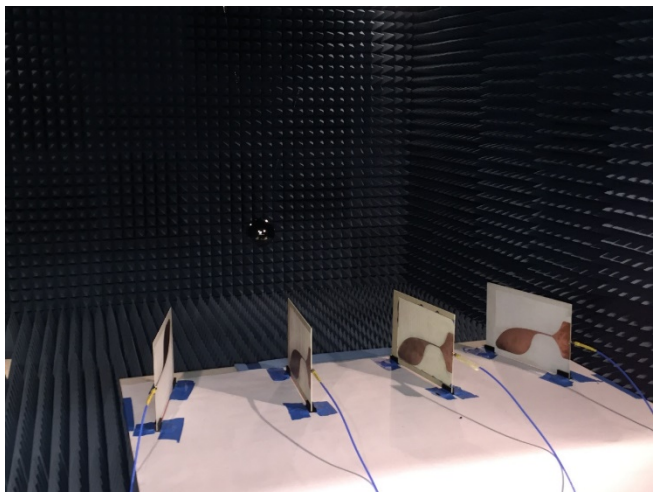

Figure 5.23: Second Experimental Setup (a) Functional Diagram (b) Anechoic Chamber Photo

The array size was reduced to four elements, and there were four antennas fabricated to be stationary in the chamber to improve repeatability between measurements. The cables for each of the antennas (L_1, L_2, L_3, L_4) are all close to equal in length to keep consistent phase progression from the antenna to the scope. A splitter is used for the mono-static measurements. The signal from the amplifier passes through port 1 of the splitter/combiner and leaves through the common port remaining isolated from the scope by 20 dB, so that that the signal does not exceed the port input power limits of the scope. The scattered response comes back through the common and half the power goes to the scope and the other half gets "reflected" back to the amp. That power is so small however that there is no risk of harming the amplifier. With the new set up we obtained the results shown in Figure 5.24.

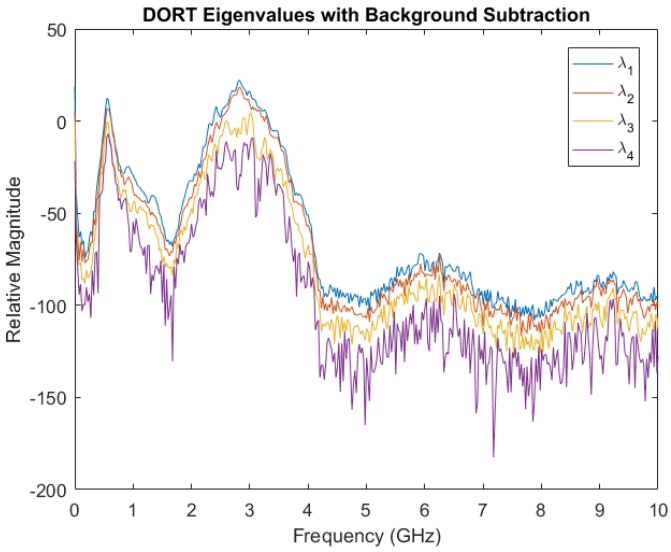

Figure 5.24: Second Experimental results

It is clear that some harmonics remain along with a 500 MHz signal; however what is most concerning is still no significant separation between eigenvalue. Up to this point, we have been looking at the eigenvalues on a dB scale. If you look at the eigenvalues on a linear scale, it is clear that we are close to resolving the target (see Figure 5.25)

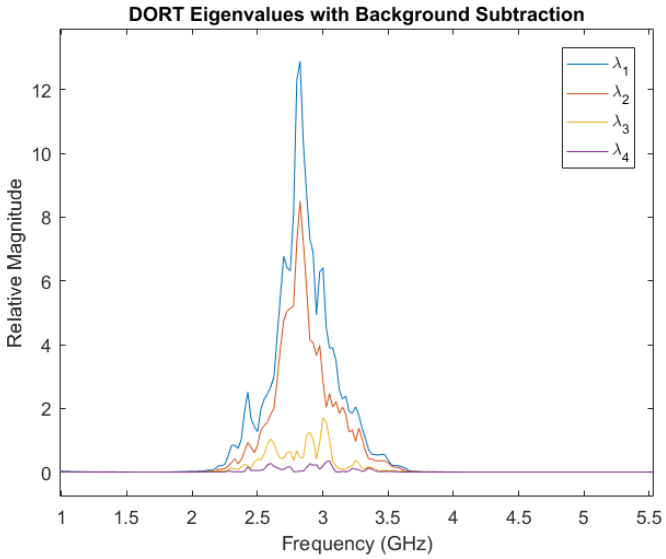

Figure 5.25: Second Experimental results linear scaling

Looking at the time domain data we can make more sense about the observation (see Figure 5.26).

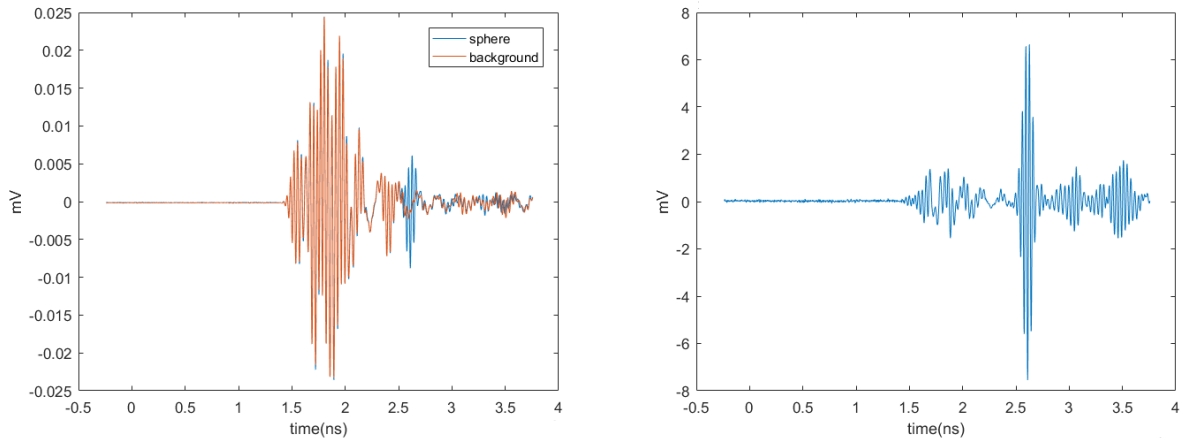

Figure 5.26: Initial bi-static result one linear target (a) raw measurement (b) background subtracted

Similar to before we can see the response of the sphere emerging from beneath the background measurement. After background subtraction, the resulting curve is plotted in Figure 5.26(b), and it is clear that the target response is greater than the other noise. To try to clean up the

data time gating was used as a means of ignoring the other artifacts in the measurement and isolating the target response only. The following eigenvalues were acquired (see Figure 5.27).

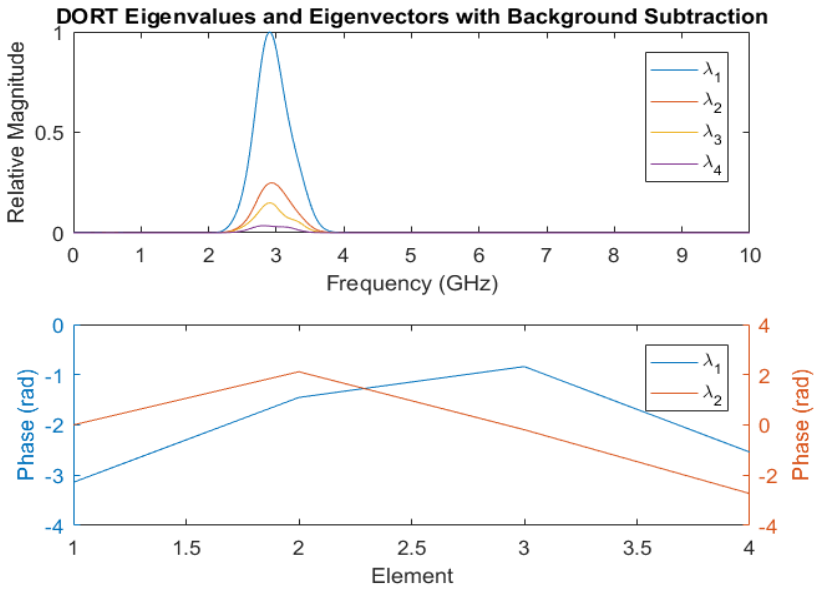

Figure 5.27: Second Experimental results linear scaling after time-gating

It appears that time-gating does a great job in cleaning up the signal and also grants significant separation between eigenvalues. It appears that a single linear target has been resolved.

While resolving the linear target was a major milestone there is still work to be done. After all, the purpose of this thesis is to detect and selectively focus waves at NL targets by identifying them by their harmonics. In the following experiment, the metal sphere was replaced with a bowtie antenna with rounded corners, but the distance to the target (down-range) was changed from 1.5 m to 60 cm see Figure 5.28.

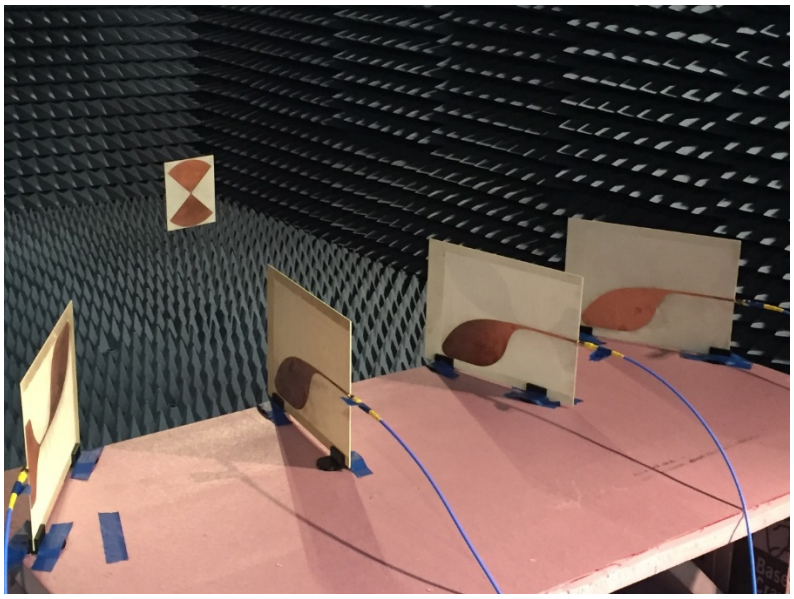

Figure 5.28: NL Experimental setup

Without employing the entire DORT method we sought to extract NL harmonics in a simple bi-static case. We were unsuccessful in turning the diode on to generate harmonics. At this point, the design of the target antenna was altered so a greater voltage was made available to the diode so that it might turn on. With the new antenna design, the harmonics can be distinguished as shown in Figure 5.29

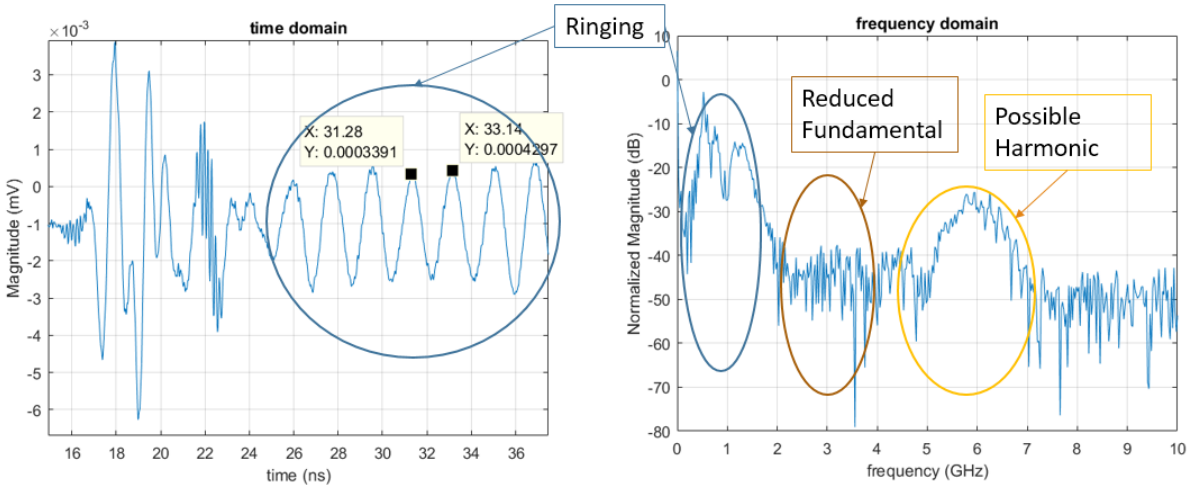

Figure 5.29: NL Bi-static test (a) time domain and (b) frequency domain

The plots shown in Figure 5.29 show the data resulting from pulse inversion. A few things to note are that there is definitely a harmonic generated at 6 GHz but also significant ringing at 500 MHz which is also visible in the time-domain. It was then determined that the 500 MHz ringing was coming from the amplifier. To clean up the signal a mini-circuits high-pass filter (passband f>2GHz) was placed on the input of the scope, and the 500 MHz ringing was resolved.

Full DORT was then performed on the single diode. The results are shown in Figure 5.30

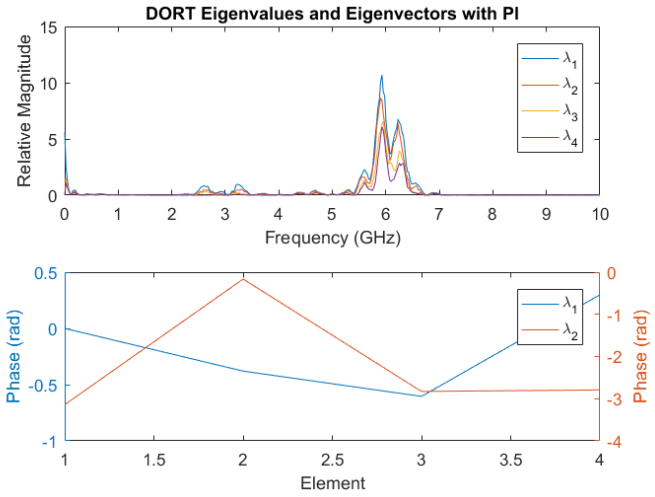

Figure 5.30: Nonlinear Experimental results in linear scaling

The eigenvalues indicate that the diode is being turned on and harmonics are generated. The 500MHz signal is eliminated; however, there seems to be some difficulty in separating the eigenvalues once again. It is again useful to look at what is going on in the time-domain.

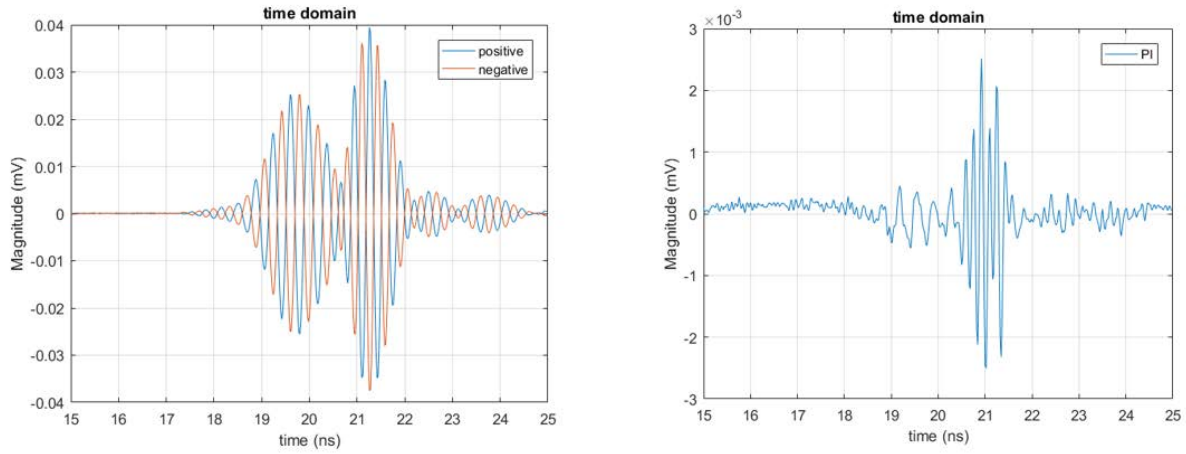

Figure 5.31: Nonlinear Experimental Bi-Static Time Domain

Nothing seems to be out of the ordinary since there is antenna coupling and a scattered response at their expected times. This was the result of a bi-static measurement, the easiest one to take. Looking at the mono-static (Figure 5.32) it is clear that a problem remains.

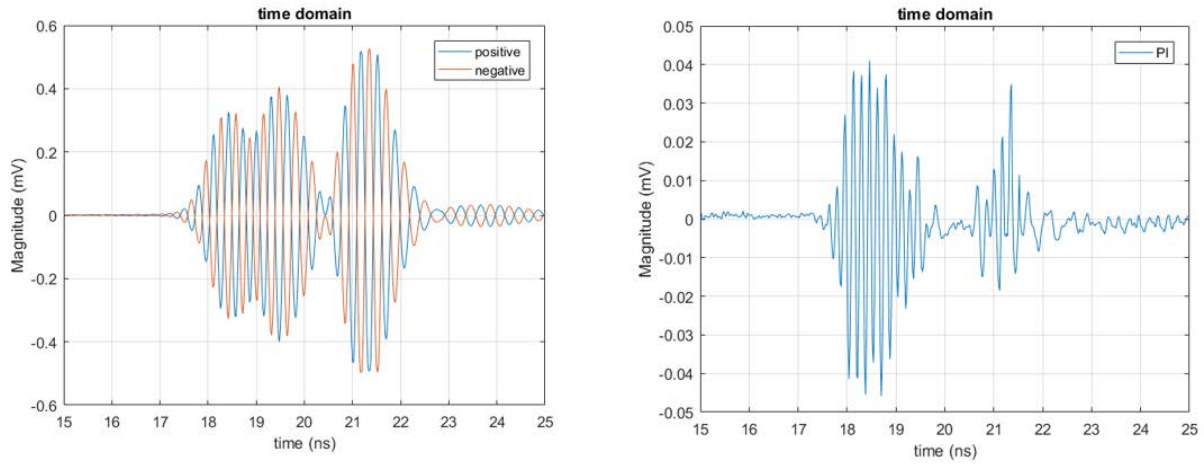

Figure 5.32: Nonlinear Experimental Mono-Static Time Domain

Harmonics are being generated by the quantization of the signal. And therefore the harmonics from mono-static are dominated by quantization rather than the harmonics from the diode. To overcome this problem a new filter is put at the input of the scope. Another high-pass with a passband which only passes signals with frequencies greater than 4GHz. It was also noticed

that there were some harmonics coming out of the amplifier. So a band-pass was placed on the output of the amplifier, and the pulse was redefined to fit the band of the filter (center frequency = 2.9 GHz with a bandwidth of 400 MHz). See Figure 5.33 for new test setup

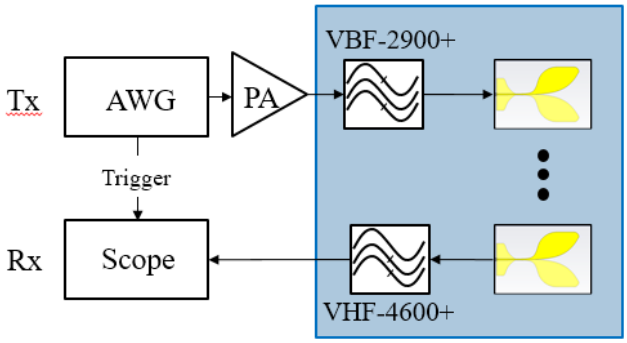

Figure 5.33: NL Experiment Setup

It is desirable that the system inside the blue area is completely linear, with the exception of the target, so the band-pass filter (Mini-circuit VBF-2900+) and the high-pass filter (Mini-circuit VHF-4600+) are used to ensure that the only harmonics that will reach the scope are physical from the diode. With the new set up we acquired the results shown below.

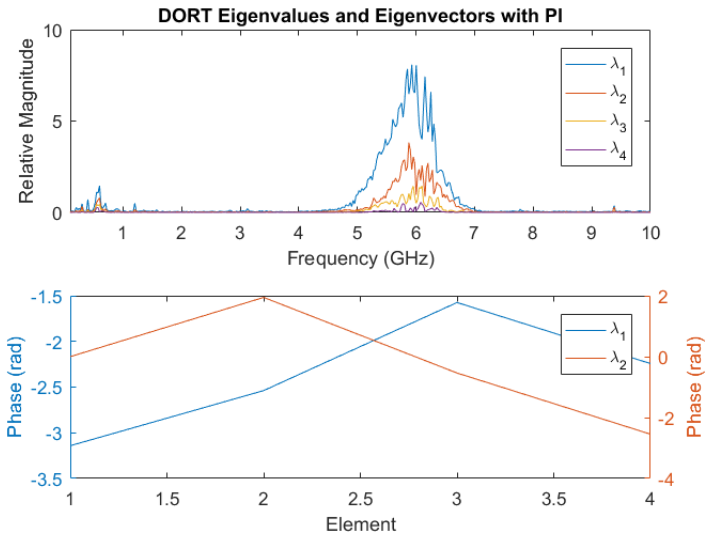

Figure 5.34: Nonlinear Experimental results in linear scaling

At this point, the results indicated that the experimental testbed was nearing completion if the eigenvalues could be separated to a greater extent. It was determined at this point that the power being reflected from the antenna in the mono-static measurements were greater than the signal received. This is due to the slight impedance mismatch of the Vivaldi antenna with the 50 W transmission line. To solve this problem, a quasi-mono-static set up was developed whereby the measurements are taken in the same procedure as bi-static which two antennas on either side of the transmit antenna and take a geometric mean of the frequency domain response of the mono-static measurement this gives us the same magnitude (assuming the magnitude doesn't change from one antenna to the other) and average phase to give the expected phase at the true mono-static point (see Figure 5.35). This procedure is called a quasi-mono-static measurement.

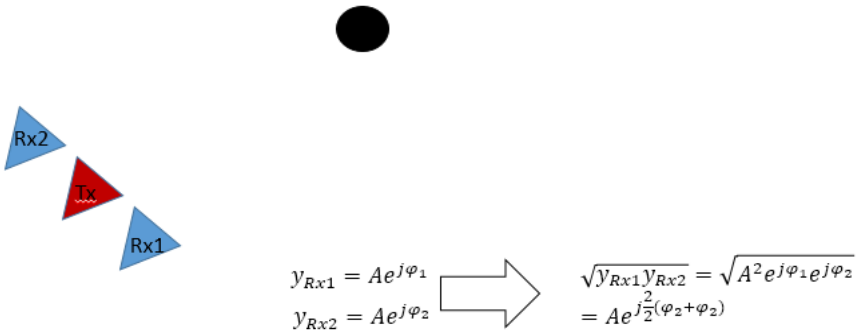

Figure 5.35: Quasi-mono-static measurement

The resulting eigenvalues from this new technique are shown in Figure 5.36

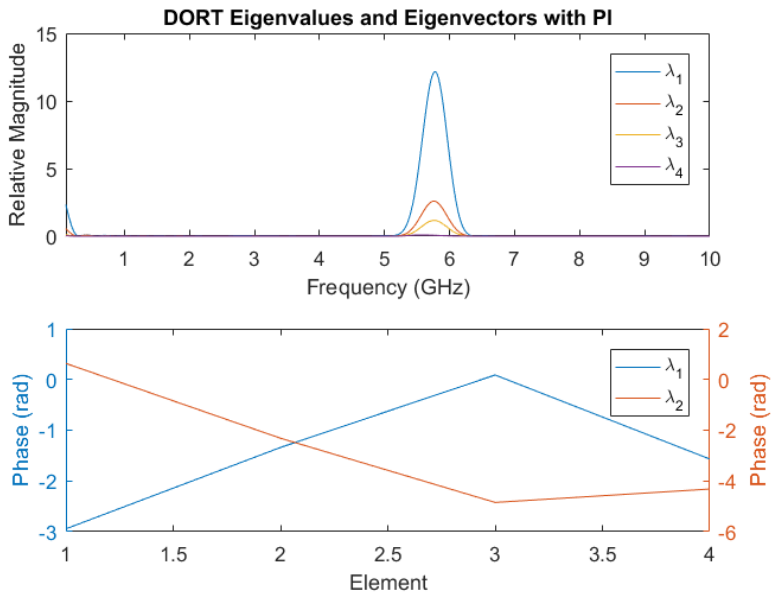

Figure 5.36: Nonlinear Experimental results in linear scaling

There appears to be great separation between eigenvalues for these NL targets; however the phase of the eigenvectors do not appear to indicate the direction of the target. It is assumed that the relative phase for each element of the eigenvector associated with the nonzero eigenvalue relates the position of the target relative to each other element. For an antenna array, this indicates the direction of the target in the environment. This assumption is only true if the given elements in the array are consistent in terms of phase progression. Slight fabrication variations in the antennas and cables can make the phases unpredictable meaning that they have no bearing on where the object is in the environment. For the experiment, it is desirable that the only source for a relative phase difference between elements is the relative path length differences from the transmit antenna to the target and back to the different elements in the array.

6. EXPERIMENTAL PI-DORT

This section serves to provide the results of combining DORT with PI to detect, locate, and focus on nonlinear elements in numerical simulation and measurement. The cases investigated for both simulation and measurement include the following:

Table 6-1: Cases Investigated for PI-DORT

Method	Case	Description
Simulation	1	Two Targets: One Linear and One Nonlinear
	2	Two Targets: Two Nonlinear
Measurement	3	One Target: Linear
	4	One Target: Nonlinear
	5	Two Targets: One Linear and One Nonlinear

Method

This section includes the finalized testbed for the experimental validation of PI-DORT. For a more comprehensive development of the testbed see Chapter 5. The interrogation array is comprised of four Vivaldi antennas with a spacing of 5 cm.

A modulated Gaussian pulse with a center frequency of 3 GHz and a -3dB bandwidth of 1GHz is generated by Matlab (see Appendix A) and transmitted by an arbitrary waveform generator (AWG), which feeds an amplifier with a gain of 40 dB and is transmitted using a Vivaldi antenna inside an anechoic chamber. The linear targets are represented by metallic spheres with a diameter of 13 cm and NL targets are represented by low turn-on voltage Schottky diodes placed at the feed-point of a bowtie antenna. The scattered response is then received by an identical Vivaldi antenna and fed into a high-speed oscilloscope. This is repeated for each element in the multi-static matrix. The data is then rearranged and the DORT operation is processed in Matlab (see Appendix B).

Results

The results for the following cases are presented here: one linear target, one NL target, one linear and one NL targets. The results also investigate using a distributed element system and a beam form array. A distributed element system is when the spacing between antennas is further than what would be considered a tightly spaced beam-forming array, and can be useful for sampling the field with greater resolution.

One Linear Target

The eigenvalues generated from DORT (see Appendix A) from one target show a clearly dominant eigenvalue (λ_1) as shown in Figure 6.1 and the phase of the eigenvectors demonstrate that the target was placed closest to the third element in the array. The smaller non-zero eigenvalues (λ_2-λ_4) may be explained by other modes introduced by the sphere since the scattering is no longer a point scatterer.

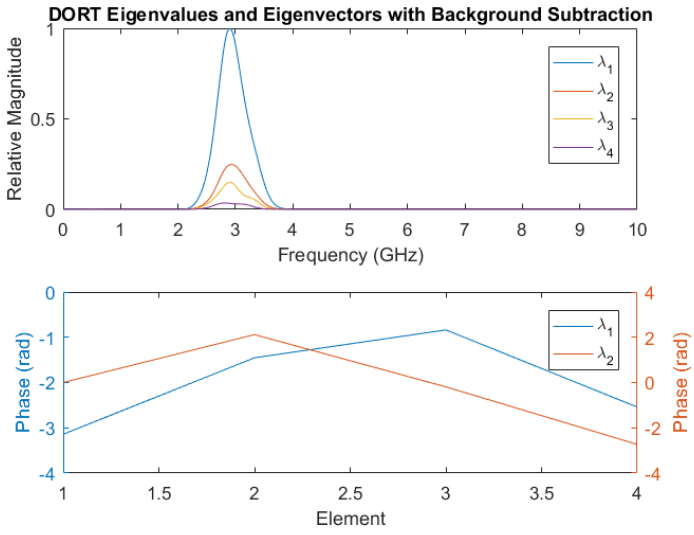

Figure 6.1: Eigenvalues and eigenvectors from one linear target.

Significant separation of the eigenvalues at 3 GHz implies one linear scatterer detected. Based on the phase of the eigenvector at 3GHz it can be seen that the target is closest to elements 2 and 3 of the array indicating that the target is located in the center of the field.

One Nonlinear Target

The eigenvalues generated from DORT (see Appendix A) from one target show a clearly dominant eigenvalue (λ_1) as shown in Figure 6.2 and the phase of the eigenvectors demonstrate that the target was placed closest to the third element in the array. The smaller non-zero eigenvalues (λ_2-λ_4) may be explained by other modes introduced by the bowtie antenna since the scattering is no longer a point scatterer.

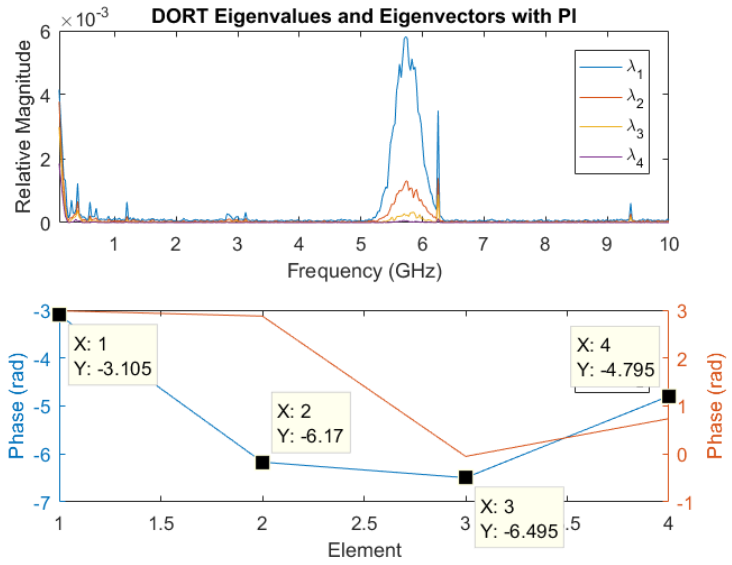

Figure 6.2: Eigenvalues and eigenvectors from one linear target.

Significant separation of the eigenvalues at 5.8 GHz implies one nonlinear scatterer detected. Based on the phase of the eigenvector at 5.8 GHz it can be seen that the target is closest to elements 2 and 3 of the array indicating that the target is located in the center of the field.

Another set of measurements were taken by using an array rather than a distributed antenna network. This is so that the beam-width of each Vivaldi antenna could cover the interrogation field. For a spacing of 5cm and using the quasi-mono-static technique described in section 5 the results for an off-centered to the left diode are shown in Figure 6.3

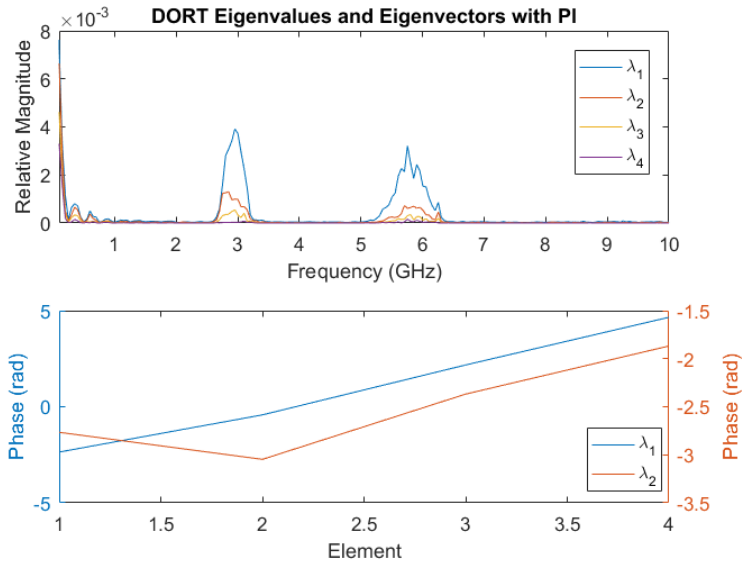

Figure 6.3: Eigenvalue and Eigenvector for off-centered diode using a closely spaced array

The results shown in Figure 6.3 show significant separation between eigenvalues at the harmonic band of 5.8 GHz. Again an explanation of why there are multiple nonzero eigenvalues is that multiple modes may be received by the array seeing that the target is extended and may not be fully resolved. At the fundamental band (2.9 GHz) there is significant suppression of the fundamental however there is no complete canceling. That being said the fundamental is suppressed enough so that the harmonic band can be discerned. The eigenvectors indicate that the target is located towards the left side of the array.

One Linear and One Nonlinear Target

Another case that was investigated was using PI-DORT with the presence of one linear target and one NL target. Using an array spacing of 5 cm, with the targets placed 1.2 m away both off center. The linear target is represented by a bowtie antenna identical to the one used for the nonlinear target. However, there is no diode soldered across the feed point. The set up can be seen in Figure 6.4

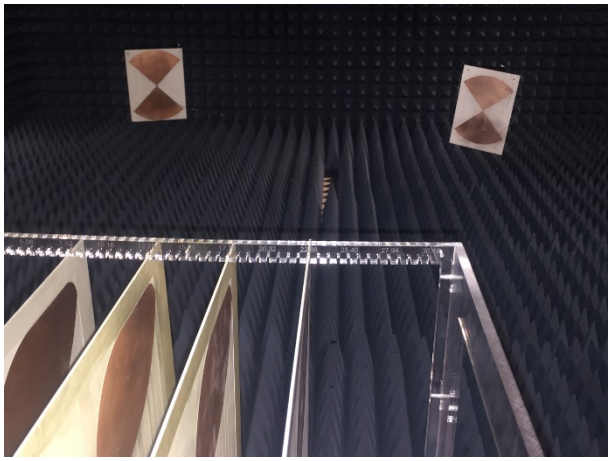

Figure 6.4: One linear and One NL experimental setup, diode is on the left and linear target is on the right

In the experimental setup, the targets were placed 1.2 m down range and the NL target resides on the left side of the array and the linear target resides on the right side of the array. Pulse inversion mitigates the effect of linear targets therefore it doesn't make sense to use pulse inversion if the location of the linear target is desired. This is why the results shown in Figure 6.5 use background subtraction.

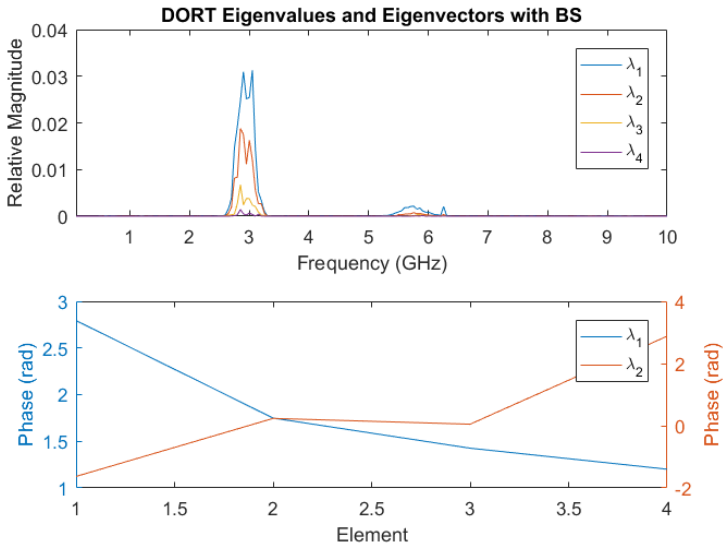

Figure 6.5: One Linear and One Nonlinear Target using Background subtraction eigenvalues

Even though the detection and location of linear targets is not important to the work reported in this thesis, these results show why combining PI and DORT is so useful. Without prior knowledge of the linear and NL target, it would be impossible to discern the two. The harmonics are also difficult to see in comparison to the fundamental response. PI-DORT is shown in Figure 6.6

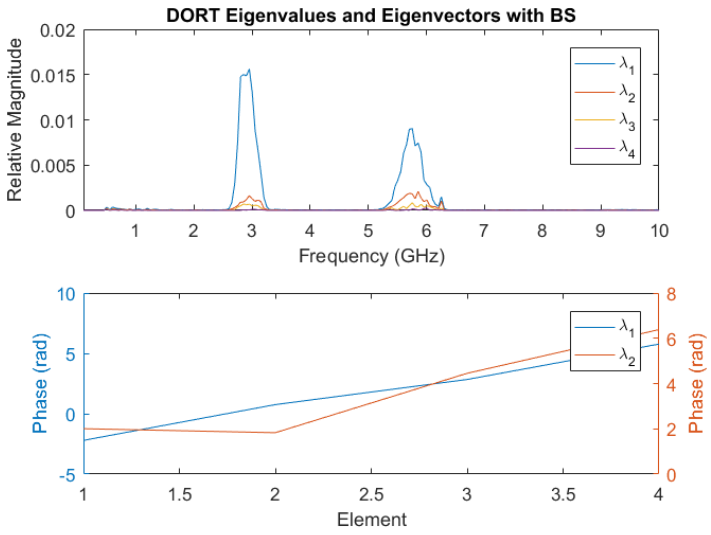

Figure 6.6: One Linear and One Nonlinear Target using PI-DORT

The fundamental frequency component is greatly reduced and the harmonics are much more visible when PI-DORT is employed. The eigenvector also shows that the nonlinear target is on the left side of the array just as the targets are set up.

Discussion

The measurements show a successful identification of NL targets. However, there are considerable components showing up in the secondary eigenvalues even when there is only one target in the environment. As discussed before the targets have an extent to them which may excite multiple modes that may appear as multiple targets.

Another cause may be the chamber itself. The chamber was designed to be anechoic at above 7 GHz and lower than that the chamber may be more reverberant. So rather than the modes being caused by an extended target the multiple-modes could be chamber modes that are excited. The root cause is difficult to know for sure.

In summary, the experiment was successful in its goal, to demonstrate PI-DORT in a 3D physical experiment. There are discernable eigenvalues with corresponding eigenvectors that have some indication of the whereabouts of the targets. The value in using PI-DORT over traditional DORT is that the harmonics from nonlinear targets become much more visible compared to the fundamental frequency, which opens the door to a variety of applications.

7. FUTURE WORK

There are several avenues for future work in PI-DORT. The work reported here provides a foundation upon which to build future investigations. Some of the limitations previously discussed can be resolved by improving the antenna design for both the target and interrogator. Also creating frequency dependent targets could greatly increase the capability of DORT and open the technique up to a variety of applications.

Addressing the Eigenvalue mixing problem

As previously reported, there are instances where targets with a different frequency response, such as linear and non-linear targets, the eigenvalue can be mixed if the most dominate scatter at one frequency is different as the most dominate scatterer at another frequency. For example, linear targets tend to scatterer a stronger fundamental than a nonlinear target. Therefore, as seen with the simulated PI-DORT results, there is a mixing of eigenvalues and eigenvectors as a function of frequency.

An algorithm can be employed which exploits a property of the eigenvectors that the eigenvectors, $\boldsymbol{V}(\omega_o)$, at a given frequency are orthogonal from one another. The eigenvectors can be seen to be orthogonal from each-other when the inner product of the two eigenvectors are identically zero, i.e.

$$\langle \boldsymbol{V}_i(\omega_o), \boldsymbol{V}_j(\omega_o) \rangle = 0 \tag{7.1}$$

In most mediums, the greens function should not experience abrupt changes in its frequency response. Therefore, the eigenstructure can be rearranged such that the adjacent frequency points of the eigenvector are correlated [9].

Furthering performance with Improved Antenna Design

Applications which can employ DORT can be practically improved with improvements on the interrogator array, and more specifically the individual antenna elements of the array. With improved directivity of an array element, the resolution of the image can be greatly improved. Attached in Appendix C is a paper describing how the gain Vivaldi antennas used could be improved by employing a spatially variant and anisotropic dielectric lens in front of the radiator.

The target antenna could also be adapted to have a wider backscattered beam-width so that the backscattered signal can be seen by a wider array. Currently, there is a lot of energy wasted because the target antenna reradiates in two directions: one direction facing the array and the other direction facing away from the array. Designing an antenna with a larger backscatter may enable the investigation of more cases where the antenna orientation and location is less important.

Frequency Signatures

For many applications, it is desirable to know more about the target than whether or not it is linear or nonlinear. For the experiment carried out in this thesis the targets were largely frequency independent in their scattering characteristics. However, it is often the case that targets of interest will have frequency characteristics. For example, a cell phone typically operates in a frequency band of 2.4 GHz while a drone may communicate at 5.8 GHz and therefore a drone and a cell phone could have drastically different frequency responses. Future work could include frequency-dependent targets where there exists a certain frequency characteristic to give the target a frequency signature to further identify the type of target that is in the environment.

A way to demonstrate this is to change the antenna design from a wide-band bow-tie antenna to a more resonant dipole antenna. A demonstration can include two targets with slightly

different length dipoles such that they can be distinguished while falling within the band of the interrogation pulse, or target antennas with DC-biased varactor diodes so the harmonic response is tunable.

Potential Applications

Once the limitations have been addressed, there are several applications that can be investigated. PI-DORT provides an answer to many difficult problems in imaging, radar, and communications. The experimental setup described in this thesis can be altered to better suit many applications which may include biomedical imaging, wireless power transfer, security and defense, and cellular communications. Chapter 8 of this thesis provides a survey of potential applications which can be investigated.

8. Survey of Applications

The detection and selective focusing at nonlinear targets have many applications including biomedical imaging, wireless power transfer, security and defense, and cellular communications. This section of the thesis provides a short survey of the possible areas of application in which PI-DORT can be utilized.

Biomedical Imaging and Microwave Thermotherapy

An application of DORT is in medical imaging. Originally DORT was utilized in ultrasound imaging of kidney stones. In order to illustrate the potential for electromagnetic imaging, consider a breast cancer tumor. If NL nanoparticle were incorporated into the tumor, PI DORT would be used to detect the presence of a tumor [9]. If the nano-particles in question were metallic, it might prove feasible via focused radiation to heat and perhaps eliminate the tumor, with much less damage to the surrounding tissue.

Wireless Power Transfer

Another application for DORT is wireless power transfer. With the rise of IoT, one hurdle is to be able to power a wireless sensor network. Broadcast towers radiate information in an omnidirectional pattern; however the device that needs the information is located at some point in the “area” that the broadcast antenna can cover; therefore, there is RF energy that is unused everywhere. There is currently a large interest in RF energy harvesting similar to solar-panels, but for lower frequencies, and with the rapid growth of low energy devices emerging on the market, the ambient energy may be enough to supply these devices.

Rectennas have nonlinear attributes to them which can be detected and DORT is a way to efficiently harvest energy for a low energy device. DORT can be a way of achieving this by selectively charging sensors without the need for human intervention

Security and Defense

DORT may be of interest for defense applications. With the rise of drones in the consumer market, it may be difficult to detect an unmanned aerial vehicle in a secure airspace. Drones within the airspace can be identified and tracked, and also if necessary a jamming signal can be sent to the drone to remove it from the airspace.

IEDs are usually triggered by cell phones. By employing PI-DORT, these cell phones can be identified as a threat or not. If the threat is deemed necessary to intervene direct high powered microwaves can be transmitted to overload the target without damaging non-threatening electronics which may be near-by.

5G Communications and IoT

There is a lot of interest in using TR for IoT and 5G communications. The reason being is TR can effectively propagate a signal from the source to the destination regardless of the environment. In fact, TR takes advantage of multipath to direct energy without the use of a massive MIMO array.

9. CONCLUSION

This thesis set out to demonstrate the detection and location of nonlinear scatterers using DORT combined with pulse inversion. Nonlinear scatterers are identified by harmonics occurring at integer multiples of the fundamental frequency of the transmit pulse. Due to the law of conservation of energy, a scattered response of the target is minuscule compared to the power transmitted by the source. Therefore the magnitude of the harmonic is also tremendously small therefore the receiver must be tuned to be sensitive enough to discern such a small scatterer. However, there exist linear scatterers in the system that exhibit large responses compared to the nonlinear scatterer. The response of the linear scatter can force the receiver outside its dynamic range, which is the range defined to be linear, and excite harmonics that interfere with the response from the nonlinear target of interest.

Pulse inversion is a technique used to cancel out the fundamental response of all targets, which allows for the receiver to discern the nonlinear scatters in an environment with linear clutter. Pulse inversion also eliminates the need to perform a background subtraction on the array. Antenna coupling is a large obstacle in performing DORT. The technique cannot resolve a single target and generates eigenvalues that are difficult to understand. Background subtraction is a technique which can resolve this by taking the multi-static response with the target data and subtracting the multi-static response with an empty environment (i.e., no targets) so that the antenna coupling is subtracted out of the multi-static matrix. However, this is in many cases impractical since the environments are typically dynamic and therefore performing a background subtraction on the array may not work. With pulse inversion performing a background subtraction is not necessary since the coupling between antennas is linear.

REFERENCES

[1] M. Fink, "Time reversed acoustics," *Phys. Today,* vol. 3, no. 50, pp. 34-40, 2004.

[2] C. Prada, S. Manneville, D. SPoliansky and M. Fink, "Decomposition of the Time Reversal Opperator: Detection and Selective Focusing on Two Scatterers," *J. Acoust. Soc. Am,* vol. 4, no. 99, pp. 2067-2076, 1996.

[3] G. Leosy, J. d. Rosney, A. Tourin, A. Derode, G. Montaldo and M. Fink, "Time Reversal of Electromagnetic Waves," *Phys. Rev. Lett.,* vol. 19, no. 92, 2004.

[4] J. Faia, K. McClintik, and S. Hong, "Application of DORT and Pulse Inversion to Detection and Selective Electromagnetic Focusing of on Nonlinear Elements," in *URSI GASS*, Montreal, 2017.

[5] E. Barbiery and M. Meo, "Time reversal DORT method applied to nonlinear elastic wave scattering," *Wave Motion,* vol. 7, no. 47, pp. 452-467, 2010.

[6] M. E. Yavuz and F. L. Teixeira, "Full Time-domain DORT for Ultrawideband Electromagnetic Fields in Dispersive, Random Inhomogenous Media," *IEEE Trans. Ant. Prop,* vol. 8, no. 54, pp. 2305-2315, 2006.

[7] T. G. Leighton, G. H. Chua, P. R. White, K. F. Tong, H. D. Giffiths and D. J. Daniels, "Radar Clutter Suppression and Target Discrimination Using Twin Inverted Pulses," *Proc. R. Soc. A,* no. 469, 2013.

[8] S. K. Hong and e. al., "Nonlinear Electromagnetic Time Reversal in an Open Semireverberant System," *Phys. Rev. Applied,* no. 2, 2014.

[9] C.-L. Hsieh, Y. Pu, R. Grange, and a. D. Psaltis, "Digital phase conjugation of second harmonic radiation emitted by nanoparticles in turbid media," *Optics Express,* vol. 18, no. 12, 2010.

[10] D. H. Simpson, C. T. Chin and P. N. Burns, "Pulse Inverson Doppler: A New Method for Detecting Nonlinear echoes from Microbubble Contrast Agents," vol. 2, no. 46, pp. 372-382, IEEE Trans. Ultrason. Ferroelect. Freq. Control.

[11] Y. Chen, F. Han, Y.-H. Yang, H. Ma, Y. Han, C. Jiang, H.-Q. Lai, D. Claffey, Z. Safar and K. J. R. Liu, "Time-Reversal Wireless Paradigm for Green Internet of Things: An Overview," *Internet of Things Journal,* vol. 1, no. 1, pp. 81-98, 2016.

[12] Y. Chen, B. Wang, Y. Han, H.-Q. Lai, Z. Safar and K. J. R. Liu, "Why Time Reversal for Future 5G Wireless?," *IEEE Signal Processing Magazine,* pp. 17-25, 2016.

[13] D. Hossain and A. S. Mohon, "Cancer Detection in Highly Dense Breasts Using Coherently Focused Time-Reversal Microwave Imaging," *IEEE Transactions on Computational Imaging,* vol. 3, no. 4, pp. 928-939, 2017.

[14] Y. Mehdi, A. Ebrahimzadeh, M. Dehmollaian and A. Madannejad, "A Time-Reversal Imaging System for Breast Screening; Theory and Initial Phantom Results," *IEEE Transactions on Biomedical Engineering,* vol. PP, no. 99, pp. 1-1, 2018.

[15] S. K. Hong, "Effect of Target Resonances on Ultrawideband-DORT," *Journal of Electromagnetic Waves and Applications,* vol. Under Review, 2018.

APPENDICES

APPENDIX A—Pulse Generation Script

```
%% Generate Wide Band Pulse %%%%%%%%%%%%%%%
%
% Author: Joseph Faia
% Last Updated: 3/2/2018
%
%%%%%%%%%%%%%%%%%%%%%%%%%%%%%%%%%%%%%%%%%%%%%%%

%% Pulse Specs
fh = 4;%GHz
fl = 2;%GHz
fo = 1e9*(fh+fl)/2;
BW = 1e9*(fh-fl)/2;
%fo = 2.9e9; %Fundemental Frequency
%BW = 2e9;   %Bandwidth 3dB
fbw = BW/fo;%Fractional Bandwidth
fs=25e9; %sample frequency
dt=1/fs; %delta time
PRF=1000e3;
T=1/PRF;
Np = 25000; % Number of points
%td = 45e-9; %time shift
td = 0; %original

PW=20e-9; %pulsewidth
N=T/dt;
t = (-N/4*dt-td):dt:(N/4*dt-td);
tt=(0:dt:dt*N);
ts = (-5e-9*dt):dt:(N*dt+5e-9*dt);

%% Generate Pulse
x = 1*gauspuls(t,fo,fbw);
y = 1*gauspuls(t,fo,fbw);
z = [x y];
z = z(1:length(tt));
plot(tt,z);

figure(2)
plot(tt,z)
Y = fft(x);
f = linspace(0,1/dt,length(t));

figure(3)
subplot(2,1,1)
plot(t*1e9-527,x); xlim([0 12]);
title('Time Domain and Frequency Domain Interrogation Pulse');
xlabel('Time (ns)'); ylabel('Normalized Magnitude');

subplot(2,1,2)
plot(f*1e-9,abs(Y)/max(abs(Y))); xlim([0 12]); %ylim([-20 0])
```

```
xlabel('Frequency (GHz)'); ylabel('Normalized Magnitude');

%% Save to .mat file for AWG

xx = [z(:,1:(length(tt)-1))';z(:,1:(length(tt)-1))'];
Waveform_Name = 'CF_3GHz_BW_1GHz_pos';
Waveform_Data = xx(1:Np);
save( [Waveform_Name '.mat'],'Waveform_Data','Waveform_Name','-v7.3');
```

APPENDIX B –PI -DORT Processing Script

```
%% Generate Wide Band Pulse %%%%%%%%%%%%%%%
%
% Author: Joseph Faia
% Last Updated: 3/2/2018
%
%%%%%%%%%%%%%%%%%%%%%%%%%%%%%%%%%%%%%%%%%%%%%%%%

clear all
clear clc
close all

N = 4;

folder = 'C:\Users\faiajm\Documents\RHIT\2016-
17\DORT\Summer2017_Thesis\Experimental
Results\DORT\Data\3_28_18\diodeL\bi-static\';
folder2 = 'C:\Users\faiajm\Documents\RHIT\2016-
17\DORT\Summer2017_Thesis\Experimental
Results\DORT\Data\3_28_18\diodeL\mono-static\';
folder3 = 'C:\Users\faiajm\Documents\RHIT\2016-
17\DORT\Summer2017_Thesis\Experimental Results\DORT\Data\2_2_17_1NL_2-
4GHz\PathComp\';

Ns = 1000;%number of samples
k = 1;
sources = 4;

%%%% Element Phase Error (rad) %%%%%%
error_a1a = 0;
error_a2a = 0.42;
error_a3a = 0.76;
error_a4a = 1.13;
%%%%%%%%%%%%%%%%%%%%%%%%%%%%%%%%%%%%%%%%%%%%%%%%

[fs, S11s, S21s,~,~] = loadsNp([folder3 'splitter.s2p'], 9, 'MA', 0);

%% IMPORT DATA
for i = 1:N
    for j = 1:N
        if(i==j)
            P(:,k) = zeros(Ns,1); Nd(:,k) = zeros(Ns,1); Bp(:,k) =
zeros(Ns,1); Bn(:,k) = zeros(Ns,1); X(:,k) = zeros(Ns,1);
            a(:,k) = zeros(Ns,1);
            myfilename_p = sprintf('p%d%da.txt',i,j);
            myfilename_n = sprintf('n%d%da.txt',i,j);
            myfilename_bp = sprintf('p%d%db.txt',i,j);
            myfilename_bn = sprintf('n%d%db.txt',i,j);
            filep = importdata([folder2, myfilename_p]);
            filen = importdata([folder2, myfilename_n]);
```

```
            filebp = importdata([folder2, myfilename_bp]);
            filebn = importdata([folder2, myfilename_bn]);

            t = filep.data(:,1);
            tt = t*1e9;

            p_a = filep.data(:,2); p_b = filebp.data(:,2);
            p_a = p_a - mean(p_a); p_a = p_a - mean(p_b);
            Pma(:,k) = p_a; Pmb(:,k) = p_b;

            n_a = filen.data(:,2); n_b = filebn.data(:,2);
            n_a = n_a - mean(n_a); n_b = n_b - mean(n_b);
            Nma(:,k) = n_a; Nmb(:,k) = n_b;

            x_a = (p_a + n_a).*heaviside(tt-7).*heaviside(11-tt);
            x_b = (p_b + n_b).*heaviside(tt-7).*heaviside(11-tt);

            Xm_a = fft(x_a); Xm_b = fft(x_b);
            Xm_a = Xm_a; Xm_b = Xm_b;
            am_a(:,k) = Xm_a; am_b(:,k) = Xm_b;

%
            k = k+1;
        else
            myfilename_p = sprintf('p%d%d.txt',i,j);
            myfilename_n = sprintf('n%d%d.txt',i,j);
            filep = importdata([folder, myfilename_p]);
            filen = importdata([folder, myfilename_n]);
            t = filep.data(:,1);
            tt = t*1e9;
            p = filep.data(:,2);
            p = p - mean(p);
            P(:,k) = p;
            n = filen.data(:,2);
            n = n - mean(n);
            Nd(:,k) = n;
            x = p+n;
            X(:,k) = x.*heaviside(tt-7).*heaviside(11-tt);
            eval(['a_temp = fft(x)*exp(sqrt(-1)*( error_a' num2str(j)
' + error_a' num2str(i) '));']);
            a(:,k) = a_temp;
            k = k+1;
        end
    end
end

%%%%Plot TD data%%%%%%
figure(1)
%plot(tt,P(:,2:4)*1e3,tt,Nd(:,2:5)*1e3);
plot(tt,X(:,2:4)*1e3);
%xlim([0 80]);
xlabel('time (ns)'); ylabel('Voltage (mV)');
```

```
title('Bi-static Measurements after PI');
legend('h21', 'h31', 'h41');
figure(2)
%plot(tt,Xma(:,1),tt,Xmb(:,1));
%xlim([0 80]);
xlabel('time (ns)'); ylabel('Voltage (mV)');
title('Bi-static TD after Background Subtraction');
legend('h11a','h11b');
%%%%%%%%%%%%%%%%%%%%%%%


%% DORT
%%%%%% convert to Freq Domain %%%%%%%
f = linspace(0,1/mean(diff(t)),length(P(:,1)));
%%%%%%%%%%%%%%%%%%% Geometric Mean for Mono-static Data%%%%%%%%%%%%%%
for jj=1:N^2
    %am_abs(:,jj) = 1/2*(abs(am_a(:,jj))+abs(am_b(:,jj)));
    am_abs(:,jj) = sqrt(abs(am_a(:,jj)).*abs(am_b(:,jj)));
    am_phase(:,jj) =
1/2*(unwrap(angle(am_a(:,jj)))+unwrap(angle(am_b(:,jj))));
    am(:,jj) = am_abs(:,jj).*exp(sqrt(-1)*am_phase(:,jj));
    Xm(:,jj) = ifft(am(:,jj),'symmetric');
     %am(:,jj) = sqrt(am_a(:,jj).*am_b(:,jj));
end

%%%%%%%%%%%%%%%%%%%%%%%%%%%%%%%%%%%%%%%

a = a + am; %Combine Mono-static and Bi-static Measurements

 for jj=1:N^2
      a(:,jj) = heaviside(f-.5e9)'.*a(:,jj); % Filter
 end
%%%%Rearrange Data Matrix%%%%%%
for k=1:sources
    for j=1:sources
        M(:,j,k)= a(:,(k-1)*N+j);
    end
end
%     t=A(:,1);
M = permute(M, [2 3 1]);
%%%%%%%%%%%%%%%%%%%%%%%%%%%%%%%%

%Frequency domain plot
figure(3)
plot(f*1e-9,abs(a(:,1:4)));xlim([0.1 10]);
xlabel('Frequency (GHz)'); ylabel('Relative Magnitude');
title('first column freq. domain');
legend('M11','M21','M31','M41')


%%%%%%%%%Apply DORT%%%%%%%%%%%%%%%
for pp=1:length(f)
```

```
    K=M(:,:,pp);
    TRO=K'*K;
    [U,L,V]=svd(K'); %%%% Singular Value Decomp.
    ss=diag(L);
    Sing(:,pp)=ss.^2;
    Us(:,:,pp)=U;

end
%%%%%%%%%%%%%%%%%%%%%%%%%%%%%%%%%%%%

%%%%%% Phase error Correcton %%%%%%%
fo_ind1 = find(f<=5.8e9,1,'last')
Us(1,:,fo_ind1)=Us(1,:,fo_ind1)*exp(sqrt(-1)*error_a1a);
Us(2,:,fo_ind1)=Us(2,:,fo_ind1)*exp(sqrt(-1)*error_a2a);
Us(3,:,fo_ind1)=Us(3,:,fo_ind1)*exp(sqrt(-1)*error_a3a);
Us(4,:,fo_ind1)=Us(4,:,fo_ind1)*exp(sqrt(-1)*error_a4a);

%%%%%%%%Plot Eig Val/Vec%%%%%%%%%%%

figure(12)
subplot(2,1,1)
plot(f*1e-9,abs(Sing)); xlim([0.1 10]);% ylim([0 6e-4]);
%plot(f*1e-9,20*log10(abs(Sing))); xlim([0.1 10]);% ylim([0 6e-4]);
xlabel('Frequency (GHz)'); ylabel('Relative Magnitude');
title('DORT Eigenvalues and Eigenvectors with PI');
legend('\lambda_1','\lambda_2','\lambda_3','\lambda_4');%,'\lambda_5',
'\lambda_6')

subplot(2,1,2)
yyaxis left
plot(1:sources,unwrap(angle(Us(:,1,fo_ind1))));
ylabel('Phase (rad)');
yyaxis right
plot(1:sources,unwrap(angle(Us(:,2,fo_ind1))));
legend('\lambda_1','\lambda_2')
xlabel('Element'); ylabel('Phase (rad)');

%%%%%%%%%%%%%%%%%%%%%%%%%%%%%%%%%%%%%%%%%%%%%%%%%%%%%%%%%%%%%%%%%%%%%%%
```

APPENDIX C—Spatially Variant Lens Paper Sent for Submission

Using a Spatially-Variant Dielectric Lens to Increase the Gain-Bandwidth of an Antipodal Vivaldi Antenna

Joseph M. Faia, *Student Member, IEEE,* John Blauert, *Student Member, IEEE,* Yuije He, Sun K. Hong, *Member, IEEE,* and Edward Wheeler, *Senior Member, IEEE*

***Abstract*—The performance of ultra-wideband techniques used in detection, sensing, communications and imaging applications can be improved by increasing the gain of the antennas employed. Lenses are means which can be used to increase antenna gain, having the advantage of offering higher gain over a wide bandwidth. If one further permits spatial variations in the lens dielectric, the effective permittivity can be made spatially and polarization dependent thus offering added flexibility in lens design. Here we report on a spatially-variant anisotropic dielectric lens which results in an increase in the gain-bandwidth of an antipodal Vivaldi antenna when compared to an antenna without a spatially-variant lens. The antennas, with and without the spatial variant lenses, have bandwidths extending from less than 10 GHz to 35 GHz. When compared with the lens without spatial variations, the anisotropic dielectric lens provides nearly the same gain to 15 GHz and an improved gain from 15 to 35 GHz.**

***Index Terms*—Antipodal Vivaldi antennas, dielectric lens, spatially-variant dielectric, ultra-wideband (UWB) antennas.**

I. Introduction

Ultra-wideband (UWB) techniques are used in areas of application including communications, detection, imaging and sensing [1, 2]. In those techniques involving antennas, modifying or increasing antenna gain can result in improved performance, added compatibility, increased resolution and enhanced capability.

In the work reported here, the use of an UWB Vivaldi antenna to explore possible improvements in antenna gain is a natural choice, since it has been widely used in UWB applications requiring a relatively high gain. The Vivaldi is an exponentially tapered slot antenna where the electric field develops an increased curvature as it propagates along the antenna's aperture, as illustrated in Fig. 1. This field "bowing" is a source of unwanted spread of the antenna's radiation pattern and which can be modified to increase the antenna's gain. One approach to increasing antenna gain would then be to modify the wave-front shape, to flatten it, through lensing.

Dielectric lenses have long been used as a means of improving gain over a range of frequencies [4]. Approaches which have been demonstrated effective in increasing the gain of Vivaldi antennas have included placing a dielectric [5-8] or else metallic patches [9, 10] in the antenna's aperture.

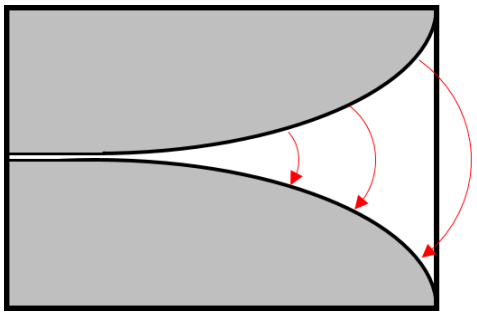

Fig. 1. Electric Field Lines on a Vivaldi antenna

This paper explores the use of a spatially-variant dielectric having an anisotropic permittivity tensor [11] which may then be exploited for wave-front shaping and gain enhancement of the antenna. The Vivaldi's quasi-2D structure allows for the proposed spatially-variant lens to be implemented with relative ease using through a simple subtractive fabrication process.

II. Antenna with Spatially-Variant Lens

The baseline antipodal Vivaldi antenna, with its two exponentially tapered conducting flares separated by a dielectric has a microstrip transmission line feed, is used here as a reference design. It is here shown in Fig. 2 with a non-spatially-variant lens with its parameters listed in Table 1.

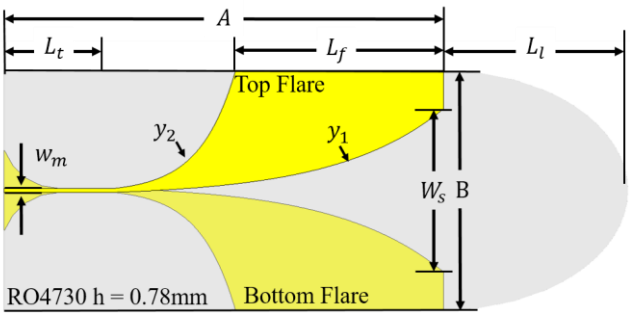

Fig. 2. Parameterized Reference Model

Manuscript received -- ,----;

J. M. Faia, Y. He and E. Wheeler are with the Department of Electrical and Computer Engineering, Rose-Hulman Institute of Technology, Terre Haute, IN 47803 USA (e-mail: wheeler@rose-hulman.edu).

J. Blauert is with the ElectroScience Laboratory, Ohio State University, Columbus, OH 43210 USA.

S. K. Hong is with the School of Electronic Engineering, Soongsil University, Seoul, 06978 South Korea (e-mail: shong215@ssu.ac.kr).

Corresponding authors: S. K. Hong and E. Wheeler.

TABLE 1
DESIGN PARAMETERS FOR REFERENCE ANTENNA

Parameter	Value (mm)
w_m	1
L_f	52
L_t	27.5
L_l	46.2
W_s	40.8
B	60
A	110

The antenna flares are defined by two exponential curves denoted by y_1 and y_2 and are defined by equations 1a through 1c.

$$y_1 = \frac{e^{\frac{x-L_t}{A-L_t}g}}{1000} - \frac{w_m}{2} \quad (1a)$$

$$y_2 = \frac{e^{\frac{x-L_t}{A-L_t}3g}}{1000} + \frac{w_m}{2} - 1 \quad (1b)$$

$$g = \ln\left(1000\left(\frac{W_s + w_m + 2}{2}\right)\right) \quad (1c)$$

Spatially-variant dielectrics can be designed and fabricated using isotropic dielectrics to yield a diagonal permittivity tensor in which the effective permittivity depends on the polarization of the electric field [11]. In designing the spatially-variant dielectric, a higher permittivity particle material is embedded in a lower-permittivity host material with the resulting permittivity tensor depending on the size, shape and orientation of the particle material. The geometric positioning of the particle material compared to the host material creates a shielding effect in the directions of low permittivity, whereas there is no shielding effect in the direction of high permittivity. In the 2D case considered here, the resulting permittivity tensor is diagonal, with two low permittivity directions and one high permittivity direction.

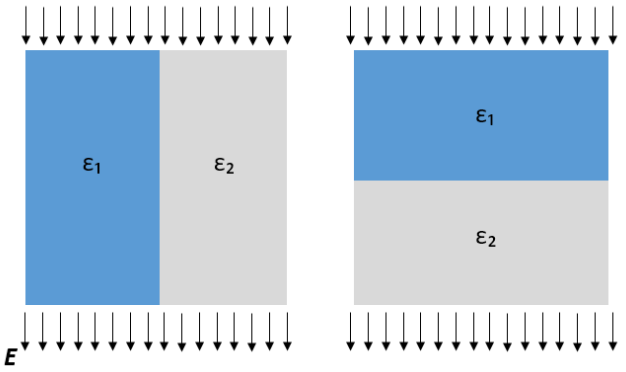

Fig. 3. Wiener Bounds use (a) parallel and (b) series capacitor analogies to calculate effective permittivity

Figure 3 shows two orientations for boundary between the host and partial material, parallel and normal to the electric field. Given equivalent potentials across Fig. 3a and Fig. 3b, it is clear that electric field in the region with higher permittivity, either ε_1 or ε_2, is greater in Fig. 3a than in Fig. 3b, thus allowing the effective permittivity in Fig. 3a to be higher than that in Fig. 3b. This can also be considered in terms of effective capacitances. Where the electric field is parallel to the boundary between the host and particle unit cell, the resulting capacitances are in parallel and, since capacitances in parallel add, the effective capacitance in Fig. 3a is higher than in Fig. 3b, thus resulting in a higher effective permittivity in Fig. 3a. In general, of course, the electric field can have any orientation to the boundaries between the two materials resulting in a diagonal permittivity tensor resulting in an effectively anisotropic dielectric, which offers a differing permittivity depending on the polarization of the electric field [12].

Spatially varying the unit cell geometry leads to a permittivity which varies as a function of position and so permits a degree of wave-guiding, which is employed here to realize a spatially-variant lens to increase the gain of an antipodal Vivaldi antenna. The direction of the higher-permittivity to be used to improve the realized gain of the antenna by orienting the material so that the electric flux is parallel to the conducting and ground planes and perpendicular to the desired direction of wave propagation. The spatially-variant lens is also observed in simulation to also reduce beam tilting and cross-polarization by creating low permittivity paths orthogonal to the desired direction of the electric flux density's preferred path.

The design incorporates anisotropic cells in the referenced elliptical dielectric lens to enhance wave-front shaping in order to improve the gain of the Vivaldi antenna. The proposed design is shown in Fig. 5.

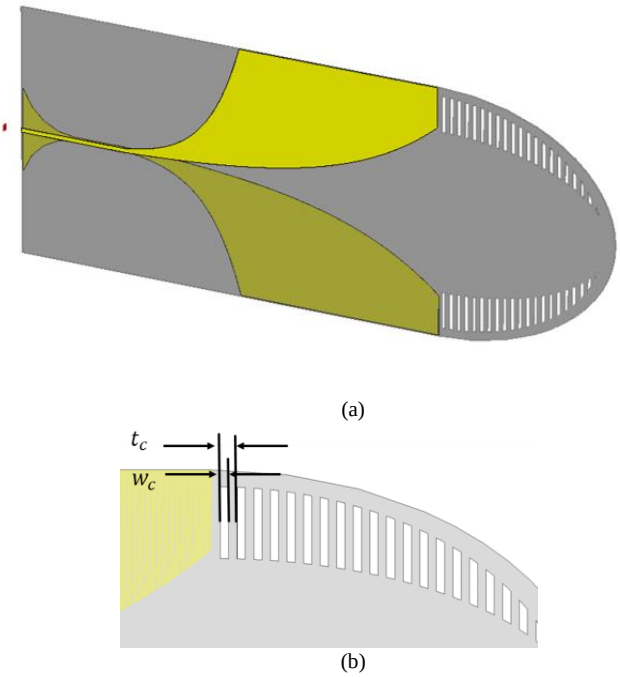

Fig. 4. (a) Proposed design with (b) anisotropic dielectric lens

Simple and inexpensive subtractive fabrication is used to mill out slots in the dielectric. The slots behave as the low permittivity host material in which the large permittivity coincides in and provides and effectively anisotropic dielectric.

III. Simulation and Measurement Results

The antennas were modeled using CST Microwave Studio and then fabricated and measured in an anechoic chamber with a vector network analyzer (VNA). The simulated and measured results are compared with those of the reference model to demonstrate improved performance.

The plot in Fig. 5 is measured return loss (S_{11}) for the reference design compared to the simulated return loss. The figure shows a radiation bandwidth, where the measured return loss is less than -10dB, from approximately 8 to 35 GHz.

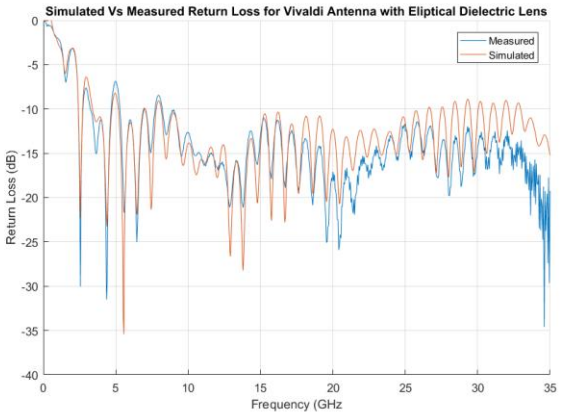

Fig. 5. Measured and Simulated Return Loss for Reference design

A useful figure of merit is the usable gain bandwidth. Here, the gain bandwidth is defined as the range of frequencies where the realized gain of the antenna is above 10dB, which sets a reasonable metric for evaluating the gain of the Vivaldi antenna.

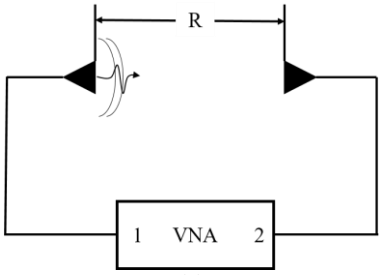

(a)

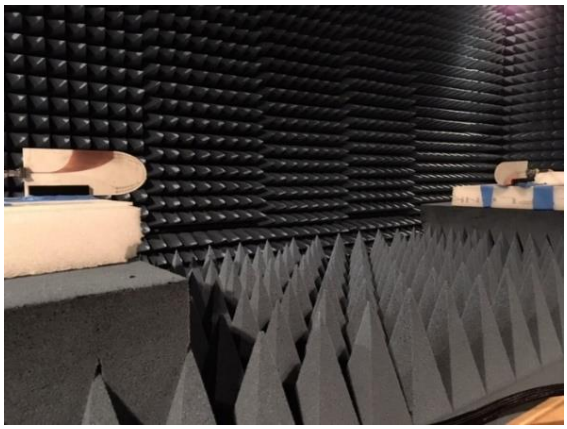

(b)

Fig. 6. Measurement Testbed (a) diagram (b) photo

To find the usable gain bandwidth the antennas were setup in an anechoic chamber placed a distance (R) apart, which puts them in the far-field of each other. Next, a VNA was used to capture the transmission from one antenna to the other (S_{21}).

Using the Friis transmission equation (2a) the gain for each antenna can be extracted by rewriting the equation shown below:

$$\frac{P_r}{P_t} = G^2\left(\frac{\lambda}{4\pi R}\right)^2 \tag{2a}$$

$$G = \left(\frac{4\pi R}{\lambda}\right)\sqrt{S_{21}}, \quad S_{21} = \frac{P_r}{P_t} \tag{2b}$$

The realized gain vs. frequency for the reference design in Fig. 7 shows a usable bandwidth spanning from 7 to 27 GHz simulated and 7 to 25 GHz measured.

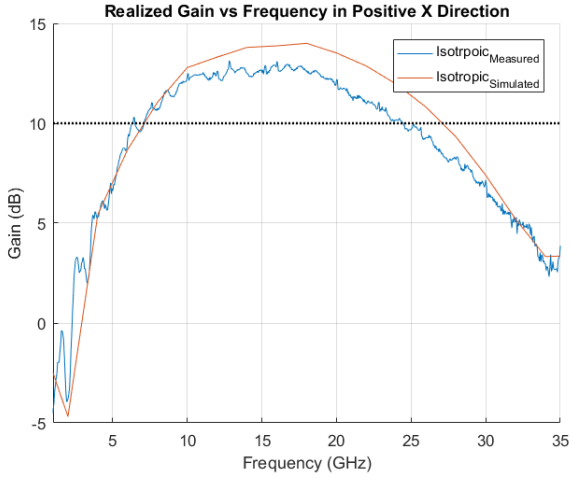

Fig. 7. Usable gain bandwidth for reference Vivaldi antennas

The return loss of the baseline antenna remains less than -10 dB through 35 GHz with its gain dropping below 10dB after 25 GHz , indicating its radiation pattern spreads somewhat at higher frequencies. This can be compared with the proposed design using a spatially-variant lens, with a return loss less than -10 dB through 35 GHz together with a gain above 10 dB through 35 GHz.

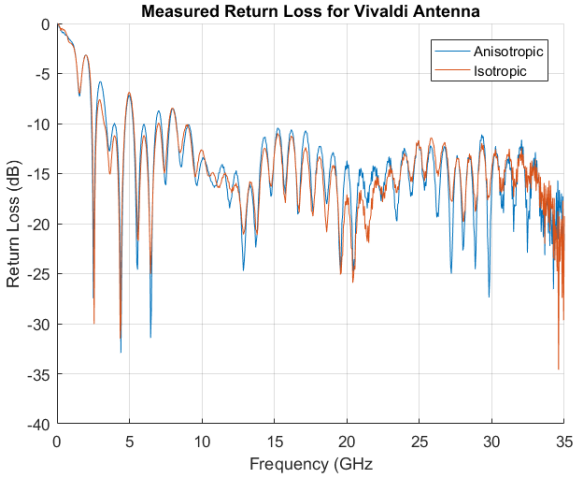

Fig. 8. Measured return loss for reference and proposed designs

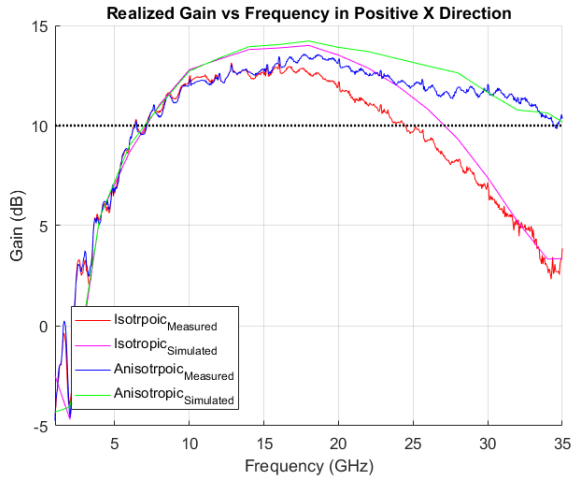

Fig. 9. Comparison of usable gain bandwidth obtained using isotropic and anisotropic lens

The anisotropic lens significantly increases the gain bandwidth of the antenna up to 35 GHz as opposed to 25 GHz for the isotropic lens. At 35 GHz the anisotropic lens provides a gain enhancement of over 6 dB to that of the isotropic lens.

IV. Conclusion

An isotropic dielectric can be made to have an effectively anisotropic permittivity by using multiple dielectrics (here we use two) and spatially varying the boundary between the two materials. This paper reports on the use of a spatially-variant dielectric as an UWB lens which shapes the wave front radiating from the Vivaldi antenna to increase the realized gain over a wider bandwidth than that observed without the spatially-variant lens to enhance its performance for detecting, sensing and imaging applications.

References

[1] M.E. Yavus and F.L. Teixeira, "Ultrawideband Microwave Sensing and Imaging Using Time-Reversal Techniques: A Review," *Remote Sensing*., vol. 9, 466-495, 2009.

[2] Y. Chen Y, Y.H. Yang, and F. Han., Time-reversal wideband communications. *IEEE Signal Process Lett*., 2013, vol. 20, no. 12, 1219-1222.

[3] Faia J.M., McClintick K.W., Hong S.K., Application of DORT and pulse inversion to detection and selective electromagnetic focusing on nonlinear elements, *32nd URSI General Assembly & Scientific Symposium (URSI-GASS)*; 2017 Aug 19-26; Montreal, Canada.

[4] S. Silver. *Microwave Antenna Theory and Design.* New York: McGraw-Hill Book Company, Inc. 1949. Print.

[5] A. Molaei, M. Kaboli, S. Mirtaheri, M. Abrishamian. "Dielectric lens balanced antipodal Vivaldi antenna with low cross-polarisation for ultra-wideband applications." *IET Microw. Antennas Propag.*, 2014, Vol. 8, Iss. 14, pp. 1137–1142.

[6] J. Borqui et al. "Balanced antipodal Vivaldi antenna with dielectric director for near-field microwave imaging." *IEEE Transactions on Antennas and Propagation*, July 2010, Vol. 58, No. 7, pp. 2318–2326.

[7] R. Goncalves, N.B. Carvalho and P. Pinho, Wireless energy transfer: Dielectric lens antenna for beam shaping in wireless-power transfer applications, 2017 *C. R. Physique*, vol. 18, pp. 78-85.

[8] G. Teni, N. Zhang, J. Qiu and P. Zhang, Research on a Novel Miniaturized Antipodal Vivaldi Antenna with Improved Radiation, *IEEE Antennas and Wireless Prop. Lett*., Vol 21, pp. 417-420.

[9] M.H.H. Agahi, H. Abiri and F. Mohajeri, Investigation of a New Idea of Antipodal Vivaldi Antenna Design, *Int. J. of Comp. and Elec. Eng*., April 2011, Vol. 3, No. 2, pp. 277-281

[10] I.T. Nassar and T.M. Weller, A Novel Method for Improving Antipodal Vivaldi Antenna Performance, July 2015, *IEEE Trans. Antennas Propag*., Vol. 63, No. 7, pp. 3321-3324,

[11] R.C. Rumpf, J.J. Pazos, J.L. Digaum, S.M. Kuebler, 2015, Spatially variant periodic structures in electromagnetics., Phil. Trans. R. Soc. A 373: 20140359.

[12] D. E. Aspens, "Local-field effects and effective-medium theory: A microscopic perspective," AM. J. Phys., vol. 50, no. 8, Aug. 1982